ELECTRO-MECHANICAL IMPEDANCE TECHNIQUE FOR STRUCTURAL HEALTH MONITORING AND NON-DESTRUCTIVE EVALUATION

Suresh Bhalla[1] and Chee-Kiong Soh[2]

[1]Assistant Professor, Department of Civil Engineering, Indian Institute of Technology Delhi, Hauz Khas, New Delhi 110 016 INDIA. Email: sbhalla@civil.iitd.ac.in
[2] Professor, School of Civil and Environmental Engineering, Nanyang Technological University, Singapore 639798.

ABSTRACT

The scientific community across the globe is thrusting significant efforts toward the development of new techniques for structural health monitoring (SHM) and non-destructive evaluation (NDE), which could be equally suitable for civil-structures, heavy machinery, aircraft and spaceships. This need arises from the fact that intensive usage combined with long endurance causes gradual but unnoticed deterioration in structures, often leading to unexpected disasters, such as the Columbia Shuttle breakdown in 2003. For wider application, the techniques should be automatic, sufficiently sensitive, unobtrusive and cost-effective. In this endeavour, the advent of the smart materials and structures and the related technologies have triggered a new revolution. Smart piezoelectric-ceramic lead zirconate titanate (PZT) materials, for example, have recently emerged as high frequency impedance transducers for SHM and NDE. In this role, the PZT patches act as collocated actuators and sensors and employ ultrasonic vibrations (typically in 30-400 kHz range) to glean out a characteristic admittance 'signature' of the structure. The admittance signature encompasses vital information governing the phenomenological nature of the structure, and can be analysed to predict the onset of structural damages. As impedance transducers, the PZT patches exhibit excellent performance as far as damage sensitivity and cost-effectiveness are concerned. Typically, their

sensitivity is high enough to capture any structural damage at the incipient stage, well before it acquires detectable macroscopic dimensions. This new SHM/ NDE technique is popularly called the *electro-mechanical impedance* (EMI) technique in the literature.

This paper describes the recent theoretical and technological developments in the field of EMI technique. PZT-structure interaction models are first described, including a new one proposed by the authors, followed by their application for structural identification and quantitative damage prediction using the extracted mechanical impedance spectra. Results from experiments on representative aerospace and civil structural components are presented. A new experimental technique developed at the Nanyang Technological University (NTU), Singapore, to predict i*n situ* concrete strength non-destructively is then described. Calibration of piezo-impedance transducers for damage assessment of concrete is covered next. Finally, practical issues such as repeatability and transducer protection are elaborated. The recent developments facilitate much broader as well as more meaningful applicability of the EMI technique for SHM/ NDE of a wide spectrum of structural systems, ranging from aerospace components to civil structures.

INTRODUCTION

Over the past two decades, several SHM and NDE techniques have been reported in the literature, based on either the global or the local interrogation of structures. The global dynamic techniques involve subjecting the structure under consideration to low frequency excitations so as to obtain the first few natural frequencies and extract the corresponding mode shapes. These are then processed to obtain information pertaining to the location and severity of the damages. Several 'quick' algorithms have been proposed to locate and quantify damages in simple structures (mostly beams) from the measured natural frequency and mode shape data. The change in curvature mode shape method (Pandey et al., 1991), the change in stiffness method (Zimmerman and Kaouk, 1994), the change in flexibility method (Pandey and Biswas, 1994) and the damage index method (Stubbs and Kim, 1994) are some of the algorithms in this category, to name a few. The main drawback of the global dynamic techniques is that they rely on relatively small number of first few structural modes, which, being global in character, are not sensitive enough to be affected by localized damages. Pandey and Biswas (1994), for example, reported that a 50% reduction in the Young's modulus of elasticity, over the central 3% length of a 2.44m long simply supported beam only led to about 3% reduction in the first natural frequency. This shows that the global parameters (on which these techniques heavily rely) are not appreciably affected by the localized damages. It could be possible that a damage large enough to be detected might already be detrimental to the health of the structure. Another limitation of these techniques is that owing to low frequency, typically less than 100Hz, the measurement data is prone to contamination by ambient noise, which too happens to be in the low frequency range.

Another category of the SHM/ NDE techniques are the local techniques, which, as opposed to the global techniques, rely on the localized interrogation of the structures. Some techniques in this category are the ultrasonic wave propagation technique, acoustic emission, magnetic field analysis, electrical methods, penetrant dye testing, impact echo testing and X-ray radiography, to name a few. McCann and Forde (2001) provided a detailed review of the local methods for SHM. The sensitivity of the local techniques is much higher than the global techniques. However, they share several drawbacks, which hinder their autonomous application for SHM, especially on large civil-structures (Giurgiutiu and Rogers, 1997, 1998; Park et al., 2000). The ultrasonic techniques, for example, are based on elastic wave propagation and reflection within the host structure's material to identify field inhomogeneities due to local damages and flaws. Their potential in identifying damage as well as for non-destructive strength characterization of concrete has been well demonstrated (Shah et al., 2000; Gudra and Stawiski., 2000). However, they need large transducers for excitation and generation of measurement data, in time domain, that requires complex processing. In addition, they involve expensive operational hardware and render the structure unavailable throughout the length of the test. Similar constraints have been pointed out for other local methods as well structures (Giurgiutiu and Rogers, 1997, 1998; Park et al., 2000). A common limitation of the local techniques is that usually, a probe or fixture needs to be physically moved around the structure for evaluation. Often, this not only prevents the autonomous application of the techniques but may also demand the removal of finishes or covers, such as false ceilings. Hence, the techniques are often applied at selected probable damage locations only (often based on past experience), which is almost tantamount to knowing the damage location *a priori*.

This paper reports on the recent theoretical and technological developments in the application of surface bonded self-sensing piezo-electric ceramic (PZT) patches working as impedance

transducers for SHM/ NDE. The PZT patches, owing to the inherent direct and converse mechatronic effects, can be utilized as impedance transducers for SHM (Park, 2000), through the measurement of admittance as a function of frequency. This technique has emerged during the last ten years only, and is commonly called the electro-mechanical impedance (EMI) technique. In principle, this technique is similar to the global dynamic techniques but its sensitivity is of the order of the local ultrasonic techniques. It employs low-cost transducers, which can be permanently bonded to the structure and can be interrogated without removal of any finishes or rendering the structure unusable. No complex data processing or any expensive hardware is warranted. The data is directly generated in the frequency domain as opposed to time domain in the ultrasonic techniques. Several proof-of-concept non-destructive SHM/NDE applications of the EMI technique have been reported in the literature. Sun et al. (1995) reported on the use of the EMI technique for SHM of a lab sized truss structure. Ayres et al. (1998) extended the study to prototype truss joints. Soh et al. (2000) established the damage detection and localization capability of the EMI technique on real-life concrete structures through a destructive load test on a prototype reinforced concrete (RC) bridge. Park et al. (2000, 2001) reported significant proof-of-concept applications of the technique on structures such as composite reinforced masonry walls, steel bridge joints and pipeline systems. The most significant observation by Park et al. (2000) was that the technique is tolerant to mechanical noise, giving it a leading edge over the conventional global dynamic methods. The next section briefly describes the fundamental piezoelectric relations and the PZT-structure interaction models, which are key in understanding the physical principles underlying the EMI technique.

PIEZOELECTRIC CONSTITUTIVE RELATIONS

Consider a PZT patch, shown schematically in Fig.1, under an electric field E_3 along direction 3 and a stress T_1 along direction 1. It is assumed that the patch expands and contracts in direction 1 when the electric field is applied in direction 3. The fundamental constitutive relationships of the PZT patch may be expressed as (Ikeda, 1990)

$$D_3 = \overline{\varepsilon_{33}^T} E_3 + d_{31} T_1 \tag{1}$$

$$S_1 = \frac{T_1}{\overline{Y_{11}^E}} + d_{31} E_3 \tag{2}$$

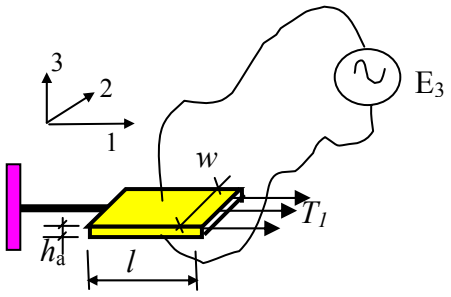

Fig. 1 A PZT patch under electric field and mechanical stress.

where S_1 is the strain along direction 1, D_3 the electric charge density or electric displacement (on top and bottom surfaces) and d_{31} the piezoelectric strain coefficient. $\overline{Y_{11}^E} = Y_{11}^E(1+\eta j)$ is the complex Young's modulus of the PZT patch in direction 1 at zero electric field, η being the mechanical loss factor. Similarly, $\overline{\varepsilon_{33}^T} = \varepsilon_{33}^T(1-\delta j)$ is the complex electric permittivity of the PZT material at zero stress, δ being the dielectric loss factor. The constants $\overline{Y_{11}^E}$ and $\overline{\varepsilon_{33}^T}$ are the relevant constants for the stress field and the electric field respectively and d_{31} is the coupling constant between the two fields. The first subscript of d_{31} signifies the direction of the electric field and the second subscript signifies

the direction of the resulting stress or strain. The complex part in $\overline{Y_{11}^{E}}$ and $\overline{\varepsilon_{33}^{T}}$ is used to take care of the mechanical and the dielectric damping as a result of the dynamic excitation. Mechanical loss is caused by the phase lag of strain behind the stress. Similarly, electrical loss is caused by the phase lag of the electric displacement behind the electric field.

Eq.(1) represents the so-called 'direct effect', that is, application of a mechanical stress produces charge on the surfaces of the PZT patch. This effect is taken advantage of in using PZT material as a sensor. Eq.(2) represents the 'converse effect', that is, application of an electric field induces elastic strain in the material. Same coupling constant d_{31} appears in both the equations.

EXISTING PZT-STRUCTURE INTERACTION MODELS

Two well-known approaches for modelling the behaviour of the PZT-based electro-mechanical systems are the static approach and the impedance approach. The static approach, proposed by Crawley and de Luis (1987), assumes frequency independent actuator force, determined from the static equilibrium and the strain compatibility between the PZT patch and the host structure. The patch, under a static electric field E_3, is assumed to be a thin bar in equilibrium with the structure, as shown in Fig. 2. One end of the patch is clamped, whereas the other end is connected to the structure, represented by its static stiffness K_s. Owing to static conditions, the imaginary component of the complex terms in the PZT constitutive relations (Eqs. 1 and 2) can be dropped. Hence, from Eq. (2), the axial force in the PZT patch can be expressed as

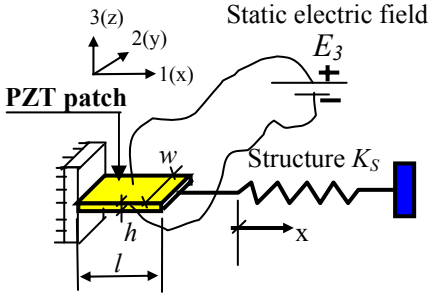

Fig. 2 Modelling of PZT-structure interaction by static approach.

$$F_P = whT_1 = wh(S_1 - d_{31}E_3)Y^E \tag{4}$$

where w denotes the width and h the thickness of the PZT patch. Similarly, the axial force in the structure can be determined as

$$F_S = -K_S x = -K_S l S_1 \tag{5}$$

where x is the displacement at the end of the PZT patch and l denotes the length of the patch. The negative sign signifies the fact that a positive displacement x causes a compressive force in the spring (the host structure). Force equilibrium in the system implies that F_P and F_S should be equal, which leads to the equilibrium strain, S_{eq}, given by

$$S_{eq} = \frac{d_{31}E_3}{\left(1 + \frac{K_S l}{Y^E wh}\right)} \tag{6}$$

Hence, from Eq. (4), the magnitude of the force in the PZT patch (or the structure) can be worked out as $F_{eq} = K_S l S_{eq}$. Now, for determining the system response under an alternating electric field, Crawley and de Luis (1987) simply recommended that a dynamic force with amplitude $F_{eq} = K_S l S_{eq}$ be considered acting upon the host structure, irrespective of the frequency of actuation. However, this is only an approximation valid under frequencies sufficiently low to give rise to quasi-static conditions. In addition, since only static PZT properties are considered, the effects of damping and inertia are not considered. Because of these reasons, the static approach often leads to significant errors, especially near the resonant frequency of the structure or the patch. (Liang et al., 1993; Fairweather 1998).

In order to alleviate the shortcomings associated with the static approach, an impedance model was proposed by Liang et al. (1993, 1994), who based their formulations on dynamic rather than static equilibrium, and rigorously considered the dynamic properties of the PZT patch as well as those of the structure. They modelled the PZT patch-host structure system as a mechanical impedance Z (representing the host structure) connected to an axially vibrating thin bar (representing the patch), as shown in Fig. 3. Considering the dynamic equilibrium of an infinitesimal element of the patch, they derived the governing differential equation as

$$\overline{Y^E}\frac{\partial^2 u}{\partial x^2} = \rho\frac{\partial^2 u}{\partial t^2} \tag{7}$$

where u is the displacement at any point on the patch in direction '1' at any instant of time t. Further, by definition, the mechanical impedance Z of the structure is related to the axial force F in the PZT patch by

$$F_{(x=l)} = whT_{1(x=l)} = -Z\dot{u}_{(x=l)} \tag{8}$$

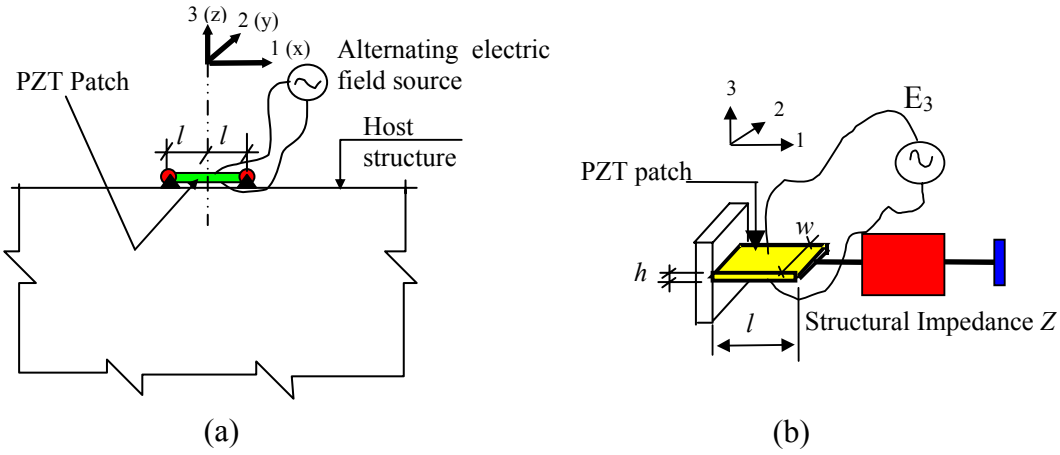

Fig. 3 Modelling PZT-structure interaction by impedance approach.

(a) A PZT patch bonded to structure under electric excitation.

(b) Model of right half of the PZT patch and host structure.

where the negative sign, as in the case of static approach, signifies the fact that a positive displacement (or velocity) causes a compressive force in the PZT patch. Further, instead of actuator's static stiffness, actuator's mechanical impedance, *Z*, was derived as

$$Z_a = \frac{\kappa w h \overline{Y^E}}{j\omega \tan(\kappa l)} \tag{9}$$

so as to rigorously include the actuator's dynamic stiffness and damping. Making use of the PZT constitutive relation (Eqs. 1 and 2), and integrating the charge density over the surface of the right half of the PZT patch (x = 0 to l), Liang and coworkers obtained the following expression for the electromechanical admittance (the inverse of electro-mechanical impedance) for the right half of the PZT patch

$$\overline{Y} = G + Bj = \omega j \frac{wl}{h}\left[(\overline{\varepsilon_{33}^T} - d_{31}^2 \overline{Y_{11}^E}) + \left(\frac{Z_a}{Z + Z_a}\right) d_{31}^2 \overline{Y_{11}^E}\left(\frac{\tan \kappa l}{\kappa l}\right)\right] \tag{10}$$

The electro-mechanical admittance of the entire PZT patch can be simply obtained by multiplying the above expression by a factor of 2. In this equation, κ is the wave number, related to the angular frequency of excitation ω, the density ρ and the complex Young's modulus of elasticity $\overline{Y^E}$ of the patch by

$$\kappa = \omega \sqrt{\frac{\rho}{\overline{Y^E}}} \tag{11}$$

As observed from Eq. (10), the electro-mechanical admittance across the terminals of the PZT patch is mathematically a complex number. *G*, the real part, is called the conductance whereas *B*, the imaginary part, is called the susceptance. A plot of G as a function of frequency is called the

conductance signature, and that of B as susceptance signature. Frequency is usually maintained in the kHz range for best results. Eq. (10) forms the basis of damage detection using the EMI

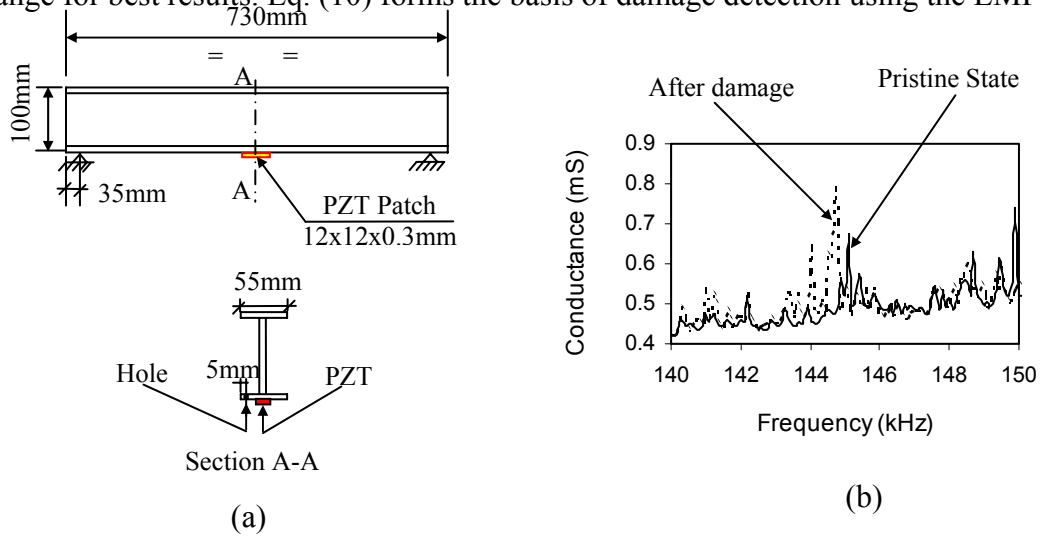

Fig. 4 (a) A steel beam instrumented with PZT patch.
(b) Effect of damage on conductance signature.

technique. Occurrence of any damage in the structure will alter the structural mechanical impedance Z, thereby changing the elecro-mechanical admittance $\overline{Y}$. This provides an indication of damage. This is illustrated in Fig. 4, which shows the effect of damage on the conductance signature of a PZT patch bonded on a steel beam. Though susceptance also undergoes change due to damage, it is somewhat feebly apparent from the raw measurements (Sun et al., 1995; Bhalla and Soh, 2003).

Eq. (10) can be decomposed into two equations- one for the real part G and another for the imaginary part B (Bhalla and Soh, 2003). G and B can be experimentally obtained at any given frequency using any commercial impedance analyzer. Hence, from Eq. (10), the structural impedance, $Z=x+yj$ can be determined (two equations and two real unknowns- x and y), as demonstrated by the authors (Bhalla and Soh, 2003). Although Liang and co-workers' model was an improvement over the static approach, the model however considers PZT patch's vibrations in one

dimension only. The formulations are thus strictly valid for skeletal structures only. In other structures, where 2D coupling is significant, Liang's model might introduce serious errors.

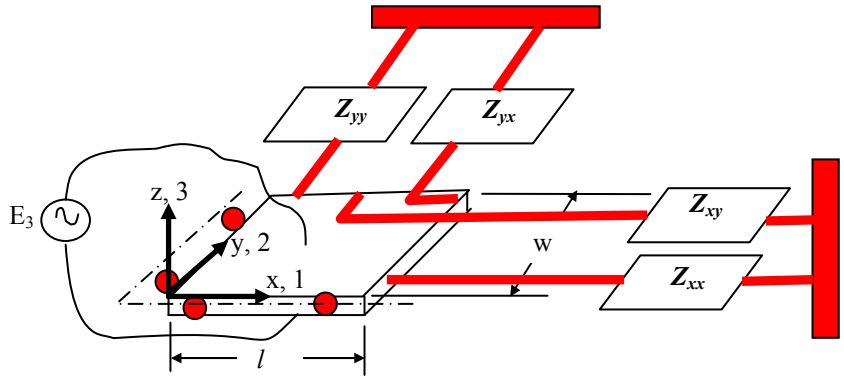

Fig. 5 Modelling PZT-structure 2D physical coupling by impedance approach (Zhou et al., 1995).

Zhou et al. (1995, 1996) extended the derivations of Liang and co-workers to model the interactions of a generic PZT element coupled to a 2D host structure. Their analytical model is schematically illustrated in Fig. 5. They represented the structural mechanical impedance by direct impedances Z_{xx} and Z_{yy} and the cross impedances Z_{xy} and Z_{yx}, related to the planar forces F_1 and F_2 (in directions 1 and 2 respectively) and the corresponding planar velocities $\dot{u}_1$ and $\dot{u}_2$ by

$$\begin{bmatrix} F_1 \\ F_2 \end{bmatrix} = -\begin{bmatrix} Z_{xx} & Z_{xy} \\ Z_{yx} & Z_{yy} \end{bmatrix} \begin{bmatrix} \dot{u}_1 \\ \dot{u}_2 \end{bmatrix} \tag{11}$$

Applying Eq. (7) along the two principal axes and imposing boundary conditions, Zhou et al. (1995) derived the following expression for the complex electro-mechanical admittance across PZT terminals

$$\overline{Y} = G + Bj = j\omega \frac{wl}{h}\left[\overline{\varepsilon_{33}^{T}} - \frac{2d_{31}^2 \overline{Y^E}}{(1-\nu)} + \frac{d_{31}^2 \overline{Y^E}}{(1-\nu)}\left\{\frac{\sin \kappa l}{l} \quad \frac{\sin \kappa w}{w}\right\} N^{-1} \begin{Bmatrix} 1 \\ 1 \end{Bmatrix}\right] \tag{12}$$

where κ, the 2D wave number, is given by

$$\kappa = \omega \sqrt{\frac{\rho(1-\nu^2)}{\overline{Y^E}}} \tag{13}$$

and N is a 2x2 matrix, given by

$$N = \begin{bmatrix} \kappa\cos(\kappa l)\left\{1-\nu\frac{w}{l}\frac{Z_{xy}}{Z_{axx}}+\frac{Z_{xx}}{Z_{axx}}\right\} & \kappa\cos(\kappa w)\left\{\frac{l}{w}\frac{Z_{yx}}{Z_{ayy}}-\nu\frac{Z_{yy}}{Z_{ayy}}\right\} \\ \kappa\cos(\kappa l)\left\{\frac{w}{l}\frac{Z_{xy}}{Z_{axx}}-\nu\frac{Z_{xx}}{Z_{axx}}\right\} & \kappa\cos(\kappa w)\left\{1-\nu\frac{l}{w}\frac{Z_{yx}}{Z_{ayy}}+\frac{Z_{yy}}{Z_{ayy}}\right\} \end{bmatrix} \tag{14}$$

where Z_{axx} and Z_{ayy} are the two components of the mechanical impedance of the PZT patch in the two principal directions, x and y respectively, derived in the same manner as in the 1D impedance approach. Although these analytical derivations are complete in themselves, experimental difficulties prohibit their direct application for extraction of host structure's mechanical impedance. As pointed out before, at a given frequency, G and B, can be measured experimentally via an impedance analyzer. To obtain complete information about the host structure, four complex unknowns- Z_{xx}, Z_{yy}, Z_{xy}, Z_{yx} (or 8 real unknowns) are needed. This is not possible using Eq. (12). Thus, the system of equations is highly indeterminate (8 unknowns with 2 equations only). As such, Zhou et al.'s model cannot be employed for experimental determination of the drive point mechanical impedance.

To alleviate the shortcomings inherent in the existing models, a new PZT-structure interaction model, based on the concept of 'effective impedance' was proposed by Bhalla and Soh (2004b). The following section describes the concept and the associated impedance model.

EFFECTIVE MECHANICAL IMPEDANCE AND ASSOCIATED MODELLING

Conventionally, the mechanical impedance at a point on the structure is defined as the ratio of the driving harmonic force (acting on the structure at the point in question) to the resulting harmonic velocity at that point. The existing models are based on this definition, the point considered being the end point of the PZT patch. The corresponding impedance is called the 'drive point mechanical impedance'. However, the fact is that the mechanical interaction between the patch and the host structure is not restricted at the PZT end points alone, it extends all over the finite sized PZT patch. Bhalla and Soh (2004a) introduced a new definition of mechanical impedance based on 'effective velocity' rather than 'drive point velocity'. In this definition, the PZT patch is assumed to be finitely sized and square shaped (half length '*l*'), surface bonded to an unknown host structure, as shown in Fig. 6. Let the patch be subjected to a spatially uniform electric field $\left(\partial E/\partial x = \partial E/\partial y = 0\right)$, undergoing harmonic variations with time. The patch's interaction with the host structure is represented by the boundary traction *f* per unit length, varying harmonically with time. This planar force causes planar deformations in the patch, leading to harmonic variations in its overall area. The 'effecive mechanical impedance' is defined as

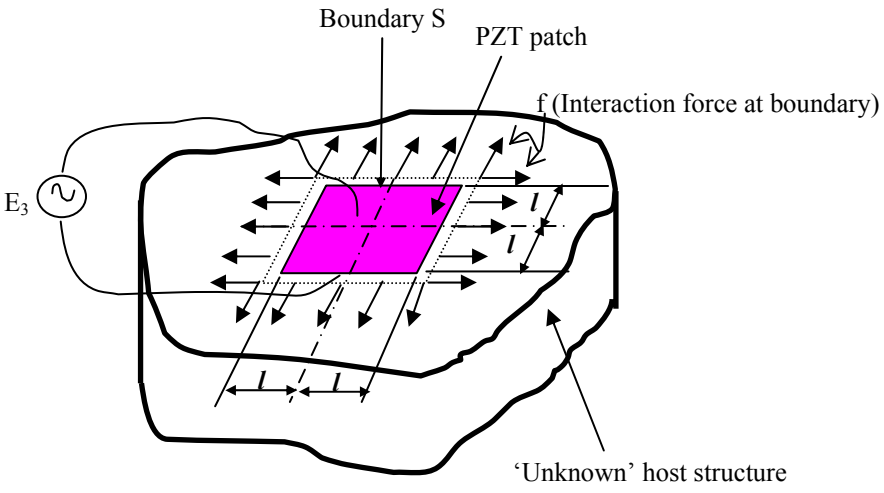

Fig. 6 A PZT patch bonded to an 'unknown' host structure.

$$Z_{a,eff} = \frac{\oint_S \vec{f}.\hat{n}\,ds}{\dot{u}_{eff}} = \frac{F}{\dot{u}_{eff}} \tag{15}$$

where $\hat{n}$ is a unit vector normal to the boundary and F represents the overall planar force (or effective force) causing area deformation of the PZT patch. $u_{eff} = \delta A/p_o$ is called the 'effective displacement', where δA represents the change in the surface area of the patch and p_o its perimeter in the undeformed condition. Differentiation of the effective displacement with respect to time yields the effective velocity, $\dot{u}_{eff}$. It should be noted that in order to ensure overall force equilibrium,

$$\oint_S \vec{f} ds = 0 \tag{16}$$

The effective drive point (EDP) impedance of the host structure can also be defined along similar lines. However, for determining the structural impedance, a planar force needs to be applied on the surface of the host structure along the boundary of the proposed location of the PZT patch.

Fig. 7 presents a close view of the interaction of one quarter of the patch with the corresponding one-quarter of host structure, taking advantage of the symmetry. Let the patch be mechanically and piezoelectrically isotropic in the x-y plane, i.e. $\overline{Y_{11}^E} = \overline{Y_{22}^E} = \overline{Y^E}$ and $d_{31} = d_{32}$. The PZT constitutive relations (Eqs. 1 and 2) can be extended to 2D case as

$$D_3 = \overline{\varepsilon_{33}^T} E_3 + d_{31}(T_1 + T_2) \tag{17}$$

$$S_1 = \frac{T_1 - \nu T_2}{\overline{Y^E}} + d_{31} E_3 \tag{18}$$

$$S_2 = \frac{T_2 - \nu T_1}{\overline{Y^E}} + d_{31}E_3 \tag{19}$$

where ν is the Poisson's ratio of the PZT material. The displacements of the PZT patch in the two principal directions are given by (Zhou et al., 1996)

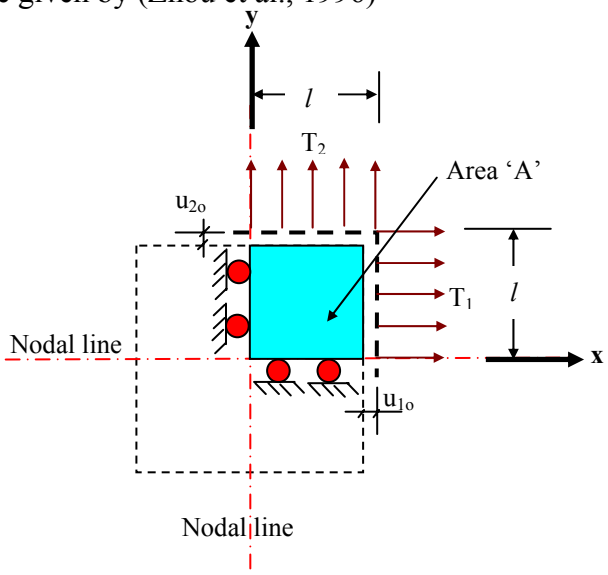

Fig. 7 A square PZT patch under 2D interaction with host structure.

$$u_1 = (A_1 \sin \kappa x)e^{j\omega t} \qquad \text{and} \qquad u_2 = (A_2 \sin \kappa y)e^{j\omega t} \tag{20}$$

where the wave number κ is given by Eq. (13), and A_1 and A_2 are the constants to be determined from the boundary conditions. The corresponding velocities can be obtained by differentiating these equations with respect to time, and the corresponding strains by differentiation with respect to the two coordinate axes, x and y. From Fig. 7, the effective displacement of the PZT patch, can be deduced as

$$u_{eff} = \frac{\delta A}{p_o} = \frac{u_{1o}l + u_{2o}l + u_{1o}u_{2o}}{2l} \approx \frac{u_{1o} + u_{2o}}{2} \tag{21}$$

where u_{1o} and u_{2o} are the edge displacements, as shown in Fig. 7. The overall planar force (or the effective force), F, is related to the EDP impedance of the host structure by

$$F = \oint_S \vec{f}.\hat{n}ds = -Z_{s,eff}\dot{u}_{eff} \tag{22}$$

The electric displacement (or the charge density) over the surface of the PZT patch can be determined from Eq. (17) by substituting $E_3 = (V_o/h)e^{j\omega t}$ and making use of Eqs. (18) and (19) as

$$D_3 = \overline{\varepsilon_{33}^T}\frac{V_o}{h}e^{j\omega t} + \frac{d_{31}\overline{Y^E}}{(1-\nu)}\left(S_1 + S_2 - 2d_{31}\frac{V_o}{h}e^{j\omega t}\right) \tag{23}$$

The instantaneous electric current, which is the time rate of change of charge, can be derived as

$$\bar{I} = \iint_A \dot{D}_3 dxdy = j\omega\iint_A D_3 dxdy \tag{24}$$

Substituting D_3 from Eq. (23), and integrating from '$-l$' to '$+l$' with respect to both x and y, the electric current can be derived as

$$\bar{I} = 4\bar{V}\omega j\frac{l^2}{h}\left[\overline{\varepsilon_{33}^T} - \frac{2d_{31}^2\overline{Y^E}}{(1-\nu)} + \frac{2d_{31}^2\overline{Y^E}}{(1-\nu)}\left(\frac{Z_{a,eff}}{Z_{s,eff}+Z_{a,eff}}\right)\left(\frac{\tan\kappa l}{\kappa l}\right)\right] \tag{25}$$

where $\bar{V} = V_o e^{j\omega t}$ is the instantaneous voltage across the PZT patch. Hence, the complex electro-mechanical admittance of the PZT patch can be obtained as

$$\bar{Y} = \frac{\bar{I}}{\bar{V}} = G + Bj = 4\omega j\frac{l^2}{h}\left[\overline{\varepsilon_{33}^T} - \frac{2d_{31}^2\overline{Y^E}}{(1-\nu)} + \frac{2d_{31}^2\overline{Y^E}}{(1-\nu)}\left(\frac{Z_{a,eff}}{Z_{s,eff}+Z_{a,eff}}\right)\left(\frac{\tan\kappa l}{\kappa l}\right)\right] \tag{26}$$

where

$$Z_{a,eff} = \frac{2\kappa l h\overline{Y^E}}{j\omega(\tan kl)(1-\nu)} \tag{27}$$

denotes the effective mechanical impedance of the PZT patch.

The main advantage of this formulation is that a single complex term for $Z_{s,eff}$ accounts for the two dimensional interaction of the PZT patch with the host structure. This makes the equation simple enough to be utilized for extracting the mechanical impedance of the structure from $\overline{Y}$, which can be measured at any desired frequency using commercially available impedance analyzers. The two unknowns, x and y in $Z_{eff} = x+yj$ can be easily determined by solving Eq. (26), which can be split into two equations, one for G and the other for B.

Further, using experimental data, Bhalla and Soh (2004b) showed that quite often, the PZT patches do not conform to ideal behaviour and therefore introduced empirical correction factors into Eq. (26), modifying it as

$$\overline{Y} = G + Bj = 4\omega j \frac{l^2}{h}\left[\overline{\varepsilon_{33}^T} - \frac{2d_{31}^2\overline{Y^E}}{(1-\nu)} + \frac{2d_{31}^2\overline{Y^E}}{(1-\nu)}\left(\frac{Z_{a,eff}}{Z_{s,eff}+Z_{a,eff}}\right)\overline{T}\right] \tag{28}$$

$$\text{where } \overline{T} = \begin{cases} \dfrac{\tan(C\kappa l)}{C\kappa l} & \text{for single-peak behaviour.} \\ \dfrac{1}{2}\left(\dfrac{\tan C_1\kappa l}{C_1\kappa l} + \dfrac{\tan C_2\kappa l}{C_2\kappa l}\right) & \text{for twin-peak behaviour.} \end{cases} \tag{29}$$

C, C_1 and C_2 are the correction factors to take into account the actual behaviour of the PZT patch. Further, the corrected actuator effective impedance (earlier expressed by Eq. 27) can be written as

$$Z_{a,eff} = \frac{2h\overline{Y^E}}{j\omega(1-\nu)\overline{T}} \tag{30}$$

For best results, it is recommended to obtain the conductance and the susceptance signatures of the PZT patch in 'free-free' condition before bonding on the host structure. This would enable determination of correct mechanical and electrical PZT parameters as well as the correction factors.

The effective impedance based electro-mechanical admittance formulations derived above were verified using the test set up shown in Fig. 8. The test structure was an aluminum block, 48x48x10mm in size, conforming to grade Al 6061-T6. Table 1 lists the major physical properties of Al 6061-T6. The test block was instrumented with a PZT patch, 10x10x0.3mm in size, conforming to grade PIC 151 (PI Ceramic, 2003). The patch was bonded to the host structure using RS 850-940 epoxy adhesive (RS Components, 2003) and was wired to a HP 4192A impedance analyzer (Hewlett Packard, 1996) via a 3499B multiplexer module (Agilent Technologies, 2003). Table 2 lists the averaged parameters of the PZT patch derived from the signatures of a group of PZT patches in 'free-free' conditions.

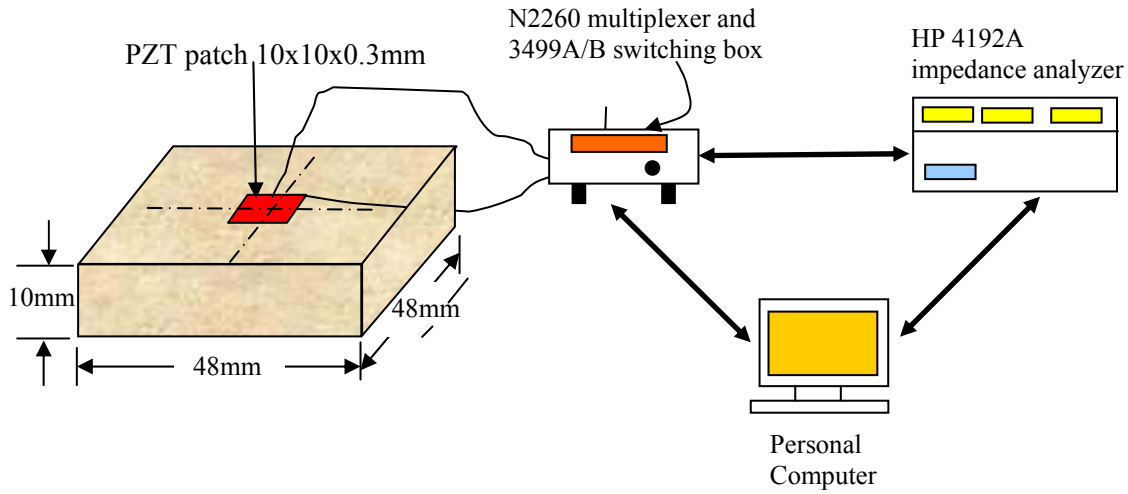

Fig. 8 Experimental set-up to verify effective impedance based new electro-mechanical formulations.

Table 1 Physical Properties of Al 6061-T6.

Physical Parameter	***Value***
Density (kg/m^3)	2715
Young's Modulus, (N/m^2)	68.95×10^9

Poisson ratio	0.33

Table 2 Averaged key parameters of PZT patches found experimentally.

Physical Parameter	***Value***
Electric Permittivity, ε_{33}^{T} (Farad/m)	1.7785×10^{-8}
Peak correction factor, C	0.898
$K = \frac{2d_{31}^2 Y^E}{(1-\upsilon)}$ (N/V^2)	5.35×10^{-9}
Mechanical loss factor, η	0.0325
Dielectric loss factor, δ	0.0224

Fig. 9 compares the experimental signatures thus obtained with those derived using Eqs.(28)-(30), as well as those using the model of Zhou and coworkers (Eqs. 12-14). The structural impedance terms were determined from the force to velocity ratio, for a given force input, using the finite element model of a quarter of the test structure shown in Fig. 10. The finite element meshing was carried out with 1.0 mm sized linear 3D brick elements, possessing three degrees of freedom at each node using the pre-processor of ANSYS 5.6 (ANSYS, 2000). Observing Figs. 9(a) and (b), it is found that the predictions by the new effective impedance model is closer to the experimental plots than those by Zhou and co-workers' model. In addition to modelling system behaviour realistically, the new formulations are much easier to apply as compared to Zhou et al.'s model. The next section describes how the new model can be employed to extract the useful information governing the mechanical behaviour of the host structure concerned.

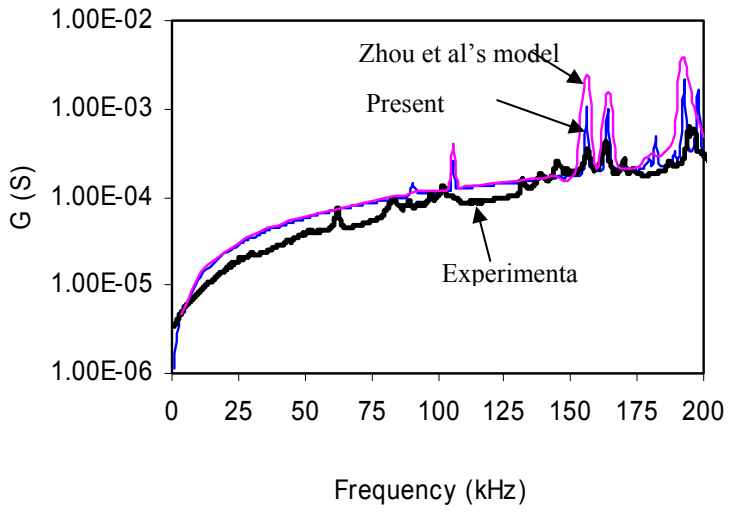

(a)

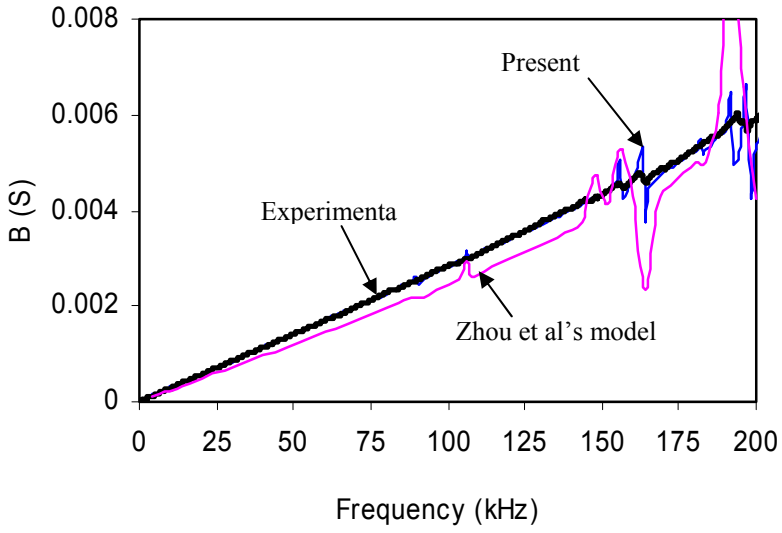

(b)

Fig. 9 Comparison between experimental and theoretical signatures.
(a) Conductance plot, (b) Susceptance plot.

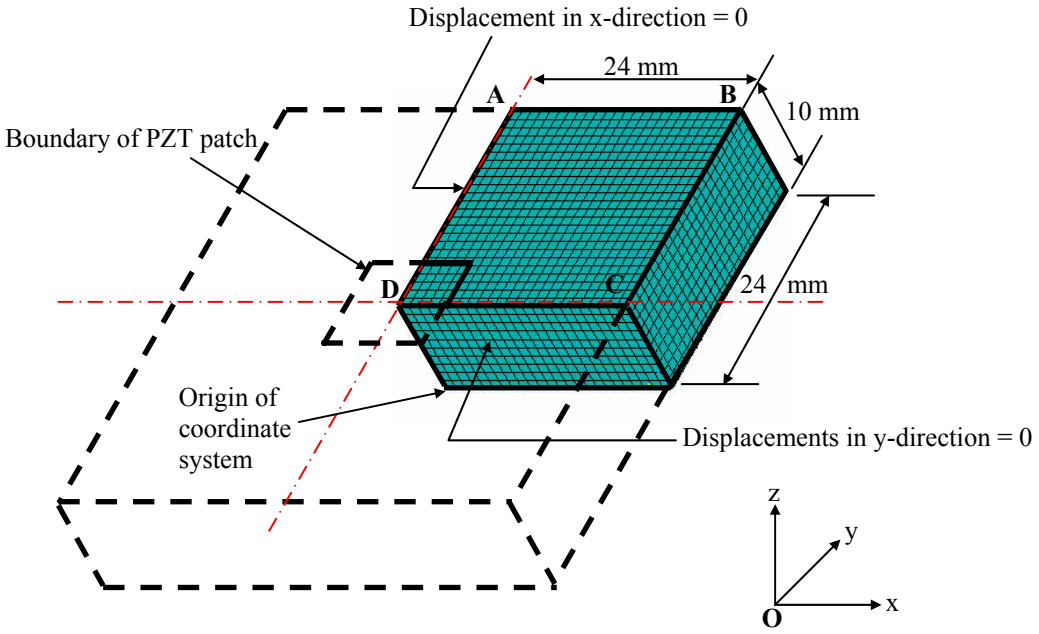

Fig. 10 Finite element model of one-quarter of test structure.

EXTRACTION OF STRUCTURAL MECHANICAL IMPEDANCE FROM ADMITTANCE SIGNATURES

The electro-mechanical admittance (given by Eq. 28) can be decomposed into two parts, I and II as

$$\bar{Y} = \underbrace{4\omega j \frac{l^2}{h}\left[\overline{\varepsilon_{33}^{T}} - \frac{2d_{31}^2 \overline{Y^E}}{(1-\nu)}\right]}_{\textbf{Part I}} + \underbrace{\frac{8\omega d_{31}^2 \overline{Y^E} l^2}{h(1-\nu)}\left(\frac{Z_{a,eff}}{Z_{s,eff}+Z_{a,eff}}\right)\overline{T}j}_{\textbf{Part II}} \tag{31}$$

It is observed that the first part solely depends on the parameters of the PZT patch. The structural parameters make their presence felt in part II only, in the form of the EDP structural impedance, $Z_{s,eff}$. Hence, Eq. (31) can be rewritten as

$$\overline{Y} = \overline{Y}_P + \overline{Y}_A \tag{32}$$

where $\overline{Y_A}$ can be termed as the 'active' component (since it is altered by any changes to the host structure) and $\overline{Y_P}$ the 'passive' component (since it is inert to any changes in the structural parameters). $\overline{Y_P}$ can be further broken down into real and imaginary parts by expanding $\overline{\varepsilon_{33}^T} = \varepsilon_{33}^T(1-\delta j)$ and $\overline{Y^E} = Y^E(1+\eta j)$ and thus can be expressed as

$$\overline{Y_P} = G_P + B_P j \tag{33}$$

where

$$G_P = \frac{4\omega l^2}{h}\left\{\delta\varepsilon_{33}^T + K\eta\right\} \tag{34}$$

$$B_P = \frac{4\omega l^2}{h}\left\{\varepsilon_{33}^T - K\right\} \tag{35}$$

and

$$K = \frac{2d_{31}^2 Y^E}{(1-\nu)} \tag{36}$$

Further,

$$\overline{Y}_A = \overline{Y} - \overline{Y}_P \tag{37}$$

or

$$\overline{Y}_A = (G + Bj) - (G_P + B_P j) \tag{38}$$

G_P and B_P can be predicted with reasonable accuracy if the conductance and the susceptance signatures of the PZT patches are recorded in 'free-free' condition, prior to their bonding to the host structures, as demonstrated by Bhalla and Soh (2004b). Thus, the active components, G_A and B_A, can be derived from the measured raw admittance signatures, G and B, as

$$G_A = G - G_P \tag{39}$$

and $$B_A = B - B_P \tag{40}$$

In complex form, the active component can be expressed as

$$\overline{Y_A} = G_A + B_A j = \frac{8\omega d_{31}^2 \overline{Y^E} l^2}{h(1-\nu)} \left(\frac{Z_{a,eff}}{Z_{s,eff} + Z_{a,eff}} \right) \overline{T} j \tag{41}$$

It was demonstrated by Bhalla et al. (2002) that the elimination of the passive component renders the admittance signatures more sensitive to structural damages. Substituting $\overline{Y^E} = Y^E(1+\eta j)$ and $\overline{T} = r + tj$ into Eq. (41), and rearranging the various terms, the equation can be simplified as

$$M + Nj = \left(\frac{Z_{a,eff}}{Z_{S,eff} + Z_{a,eff}} \right) (R + Sj) \tag{42}$$

where $$M = \frac{B_A h}{4\omega K l^2} \quad \text{and} \quad N = -\frac{G_A h}{4\omega K l^2} \tag{43}$$

and $$R = r - \eta t \quad \text{and} \quad S = t + \eta r \tag{44}$$

Further, expanding $Z_{S,eff} = x + yj$ and $Z_{a,eff} = x_a + y_a j$, and upon solving, the real and the imaginary components of the EDP structural impedance can be obtained as

$$x = \frac{M(x_a R - y_a S) + N(x_a S + y_a R)}{M^2 + N^2} - x_a \tag{45}$$

$$y = \frac{M(x_a S + y_a R) - N(x_a R - y_a S)}{M^2 + N^2} - y_a \tag{46}$$

The simple computational procedure outlined above enables the determination of the drive point mechanical impedance of the structure, $Z_{s,eff} = x + yj$, at a particular frequency ω, from the experimentally measured conductance (G) and susceptance (B). Following this procedure, 'x' and 'y' can be determined for the entire frequency range of interest. This procedure was employed to extract the structural EDP impedance of the test aluminium block (Fig. 8). Fig. 11 shows a plot of

$|Z_{eff}|^{-1}$, worked out by this procedure, comparing it with the plot determined using FEM (using Eq. 22, by applying an arbitrary planar force to the structure and determining the corresponding velocities), as discussed in the preceding sections. Reasonable agreement can be observed between the two. The main reason for plotting $|Z_{s,eff}|^{-1}$ (instead of $Z_{s,eff}$) is that the resonant frequencies can be easily identified as peaks of the plot. The next section presents a simple procedure to derive system parameters from the structural EDP impedance.

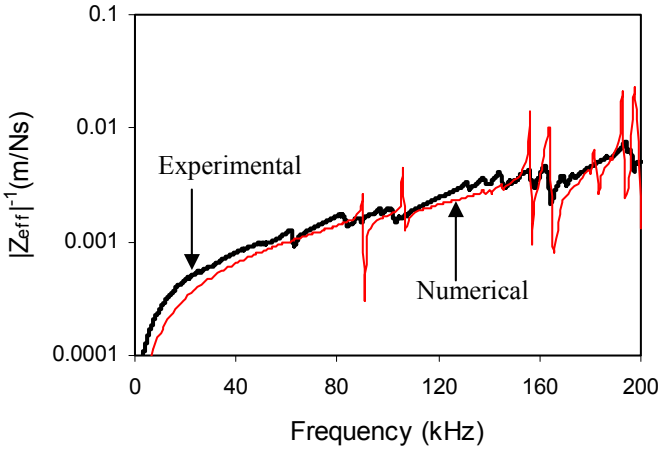

Fig. 11 Comparison between $|Z_{eff}|^{-1}$ obtained experimentally and numerically.

SYSTEM PARAMETER IDENTIFICATION FROM EXTRACTED IMPEDANCE SPECTRA

The structural EDP impedance, extracted by means of the procedure outlined in the previous section, carries information about the dynamic characteristics of the host structure. This section presents a general approach to 'identify' the host structure by means of the EDP impedance. Before considering any real-life structural system, it would be a worthwhile exercise to observe the impedance pattern of few simple systems. Fig. 12 shows the plots of the real and the imaginary

components of the mechanical impedance of basic structural elements- the mass, the spring and the damper. These elements can be further combined in a number of ways (series, parallel or a mixture) to evolve complex mechanical systems. For a parallel combination of 'n' mechanical systems, the equivalent mechanical impedance is given by (Hixon, 1988)

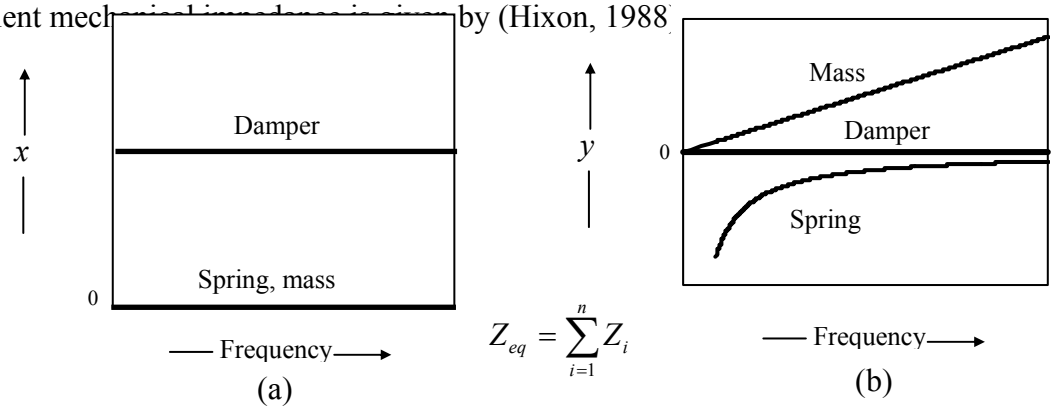

$$Z_{eq} = \sum_{i=1}^{n} Z_i \tag{47}$$

Fig. 12 Impedance plots of basic structural elements- spring, damper and mass. (a) Real part (x) vs frequency. (b) Imaginary part (y) vs frequency.

Similarly, for a series combination,

$$\frac{1}{Z_{eq}} = \sum_{i=1}^{n} \frac{1}{Z_i} \tag{48}$$

Table 3 shows the impedance plots (x and y vs frequency) for some combinations of these basic elements, determined using Eqs. (47) and (48) (Hixon, 1988). By observing the pattern of the extracted mechanical impedance (x and y vs frequency), the 'unknown' structure can be idealized as an 'equivalent lumped' system (series or parallel combination of basic elements), such that the experimental plots match those of the idealized system. To illustrate this approach, consider an aluminum block (grade Al 6061-T6), 50x48x10mm in size, representing an unknown structural system. A PZT patch 10x10x0.3mm in size, was bonded to the surface of this specimen. Experimental set-up similar to that shown in Fig. 8 was employed to acquire the admittance

signatures (conductance and susceptance) of this PZT patch. The structural EDP impedance was extracted as outlined in the preceding section. A close examination of the extracted impedance components in the frequency range 25-40 kHz suggested that the system response was similar to a parallel spring-damper (*k*-*c*) combination (system 1 in Table 3), for which

Table 3 Mechanical impedance of combinations of spring, mass and damper.

No.	COMBIN—ATION	x	y	x vs Freq.	Y vs Freq.
1	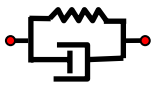	c	$-\frac{k}{\omega}$	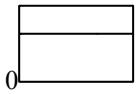	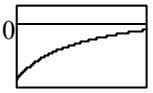
2	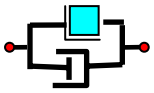	c	$m\omega$	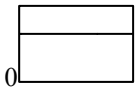	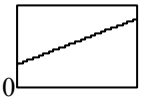
3	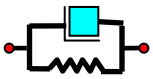	0	$m\omega-\frac{k}{\omega}$	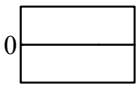	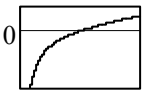
4	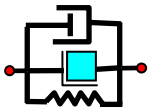	c	$m\omega-\frac{k}{\omega}$	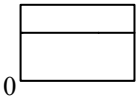	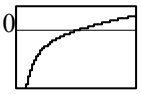
5		$\frac{c^{-1}}{c^{-2}+(\omega/k-1/\omega m)^2}$	$\frac{-(\omega/k-1/\omega m)}{c^{-2}+(\omega/k-1/\omega m)^2}$	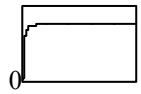	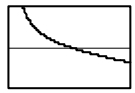
6		$\frac{c^{-1}}{c^{-2}+(\omega m)^{-2}}$	$\frac{m^{-1}-k(c^{-2}+\omega^{-2}m^{-2})}{\omega\left[c^{-2}+(\omega m)^{-2}\right]}$		
7		$\frac{c^{-1}}{c^{-2}+(\omega/k)^2}$	$\frac{\omega\left[m(c^{-2}+\omega^2k^{-2})-k^{-1}\right]}{c^{-2}+(\omega/k)^2}$	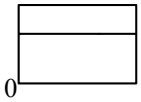	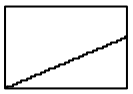
8	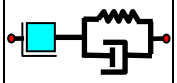	$\frac{cm^2\omega^2}{c^2+(\omega m-k/\omega)^2}$	$\frac{m\omega\left[c^2-\frac{k}{\omega}(\omega m-k/\omega)\right]}{c^2+(\omega m-k/\omega)^2}$	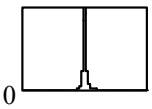	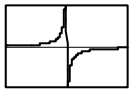

$$x = c \qquad \text{and} \qquad y = -\frac{k}{\omega} \tag{49}$$

From the extracted values of x and y, the average lumped system parameters were computed as: c = 36.54 Ns/m and k = 5.18×10^7 N/m. The analytical plots of 'x' and 'y', obtained using these equivalent parameters, match well with their experimental counterparts, as shown in Fig. 13.

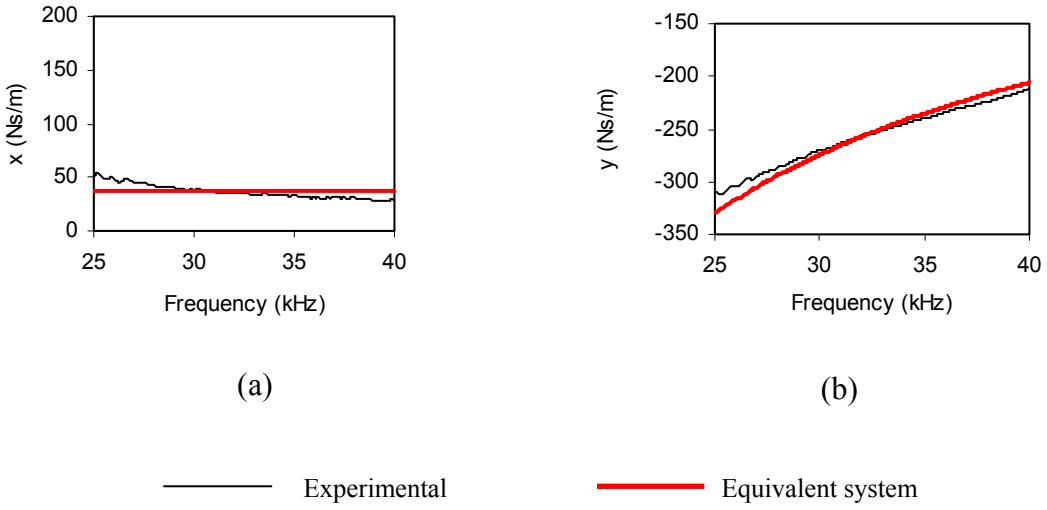

Fig. 13 Mechanical impedance of aluminium block in 25-40 kHz frequency range. The equivalent system plots are obtained for a parallel spring-damper combination. (a) Real part (x) vs frequency.(b) Imaginary part (y) vs frequency.

Similarly, in the frequency range 180-200 kHz, the system behaviour was found to be similar to a parallel spring-damper (k-c) combination, in series with mass 'm' (system 8 in Table 3). For this combination, x and y are given by (Hixon, 1988)

$$x = \frac{cm^2\omega^2}{c^2 + \left(m\omega - \frac{k}{\omega}\right)^2} \qquad \text{and} \qquad y = \frac{m\omega\left[c^2 - \frac{k}{\omega}\left(m\omega - \frac{k}{\omega}\right)\right]}{c^2 + \left(m\omega - \frac{k}{\omega}\right)^2} \tag{50}$$

and the peak frequency of the x-plot is given by

$$\omega_o = \sqrt{\frac{k}{m - \frac{c^2}{k}}} \tag{51}$$

If $x = x_o$ (the peak magnitude) at $\omega = \omega_o$ and $x = x_1$ (somewhat less than the peak magnitude) at $\omega = \omega_1 (< \omega_o)$, then using Eqs. (48) and (49), the system parameters can be determined as

$$m = \left[\frac{-B \pm \sqrt{B^2 - 2AC}}{2A}\right]^{1/2} \tag{52}$$

$$c = \frac{m^2\omega_o^2 x_o}{x_o^2 + m^2\omega_o^2} \tag{53}$$

$$k = \frac{x_o c}{m} \tag{54}$$

where

$$A = \omega_o^4\omega_1^4(x_1 - x_o) \tag{55}$$

$$B = 2x_1\omega_o^2\omega_1^2x_o^2(\omega_1^2 - \omega_o^2) + \omega_o^4\omega_1^2x_o^2x_1 - \omega_o^2\omega_1^4x_o^3 \tag{56}$$

$$C = (\omega_1^2 - \omega_o^2)^2 x_o^4 x_1 \tag{57}$$

A set of system parameters c = 1.1x10^{-3} Ns/m, k = 4.33 x 10^5 N/m and m = 3.05 x 10^{-7} kg produced similar impedance pattern, as shown in Fig. 14. Further refinement was achieved by adding a spring K^* = 7.45x10^7 N/m and a damper C^* = 12.4 Ns/m in parallel, to make the equivalent system appear as shown in Fig. 15. Hence, Eq. (48) may be refined as

$$x = C^* + \frac{cm^2\omega^2}{c^2 + \left(m\omega - \frac{k}{\omega}\right)^2} \quad \text{and} \quad y = \frac{m\omega\left[c^2 - \frac{k}{\omega}\left(m\omega - \frac{k}{\omega}\right)\right]}{c^2 + \left(m\omega - \frac{k}{\omega}\right)^2} - \frac{K^*}{\omega} \tag{58}$$

Fig. 16 shows the comparison between the experimental plots and the analytical plots. Extremely good agreement can be observed between the plots obtained experimentally and those pertaining to the equivalent lumped system. Hence, the structural system is identified with reasonably good accuracy. The next section explains how this methodology can be used to evaluate damages in aerospace and mechanical structures.

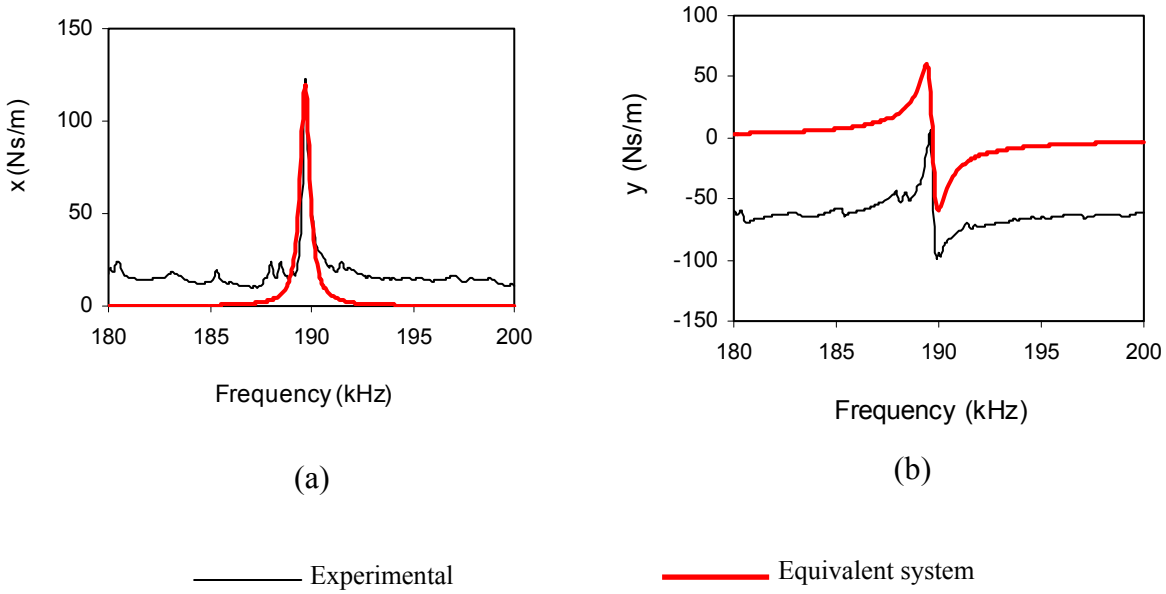

Fig. 14 Mechanical impedance of aluminium block in 180-200 kHz frequency range. The equivalent system plots are obtained for system 8 of Table 3.
(a) Real part. (b) Imaginary part.

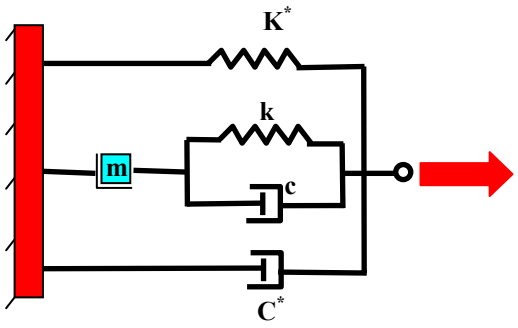

Fig. 15 Refinement of equivalent system by introduction of additional spring K^* and additional damper C^*.

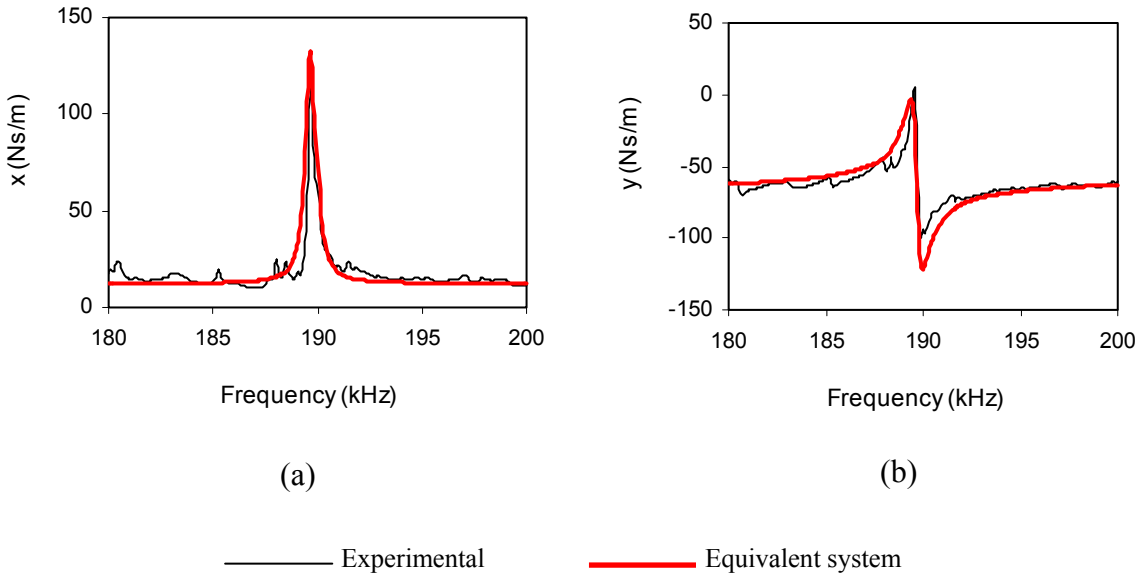

Fig. 16 Mechanical impedance of aluminium block in 180-200 kHz frequency range for refined equivalent system (shown in Fig. 15)

(a) Real part. (b) Imaginary part.

DAMAGE DIAGNOSIS OF AEROSPACE AND MECHANICAL SYSTEMS

This section describes a damage diagnosis study carried out on an aluminium block, 50x48x10mm in size, that was identified using a piezo-impedance transducer bonded on the surface. This is a typical small-sized rigid structure, characterized by high natural frequencies in the kHz range. Several critical aircraft components, such as turbo engine blades, are small and rigid, characterized by typically high natural frequencies in the kHz range (Giurgiutiu and Zagrai, 2002), and hence exhibit similar dynamic behaviour.

Damage was induced in this structure by drilling holes, 5mm in diameter, through the thickness of the specimen. Three different levels of damage were induced- incipient, moderate and severe, as shown in Figs. 17(b), 17(c), and 17(d) respectively. The number of holes was increased from two to eight in three stages, so as to simulate a gradual growth of damage from the incipient level to the severe level. After each damage, the admittance signatures of the PZT patch were recorded and the inherent structural parameters were identified in 25-40 kHz and 180-200 kHz frequency ranges.

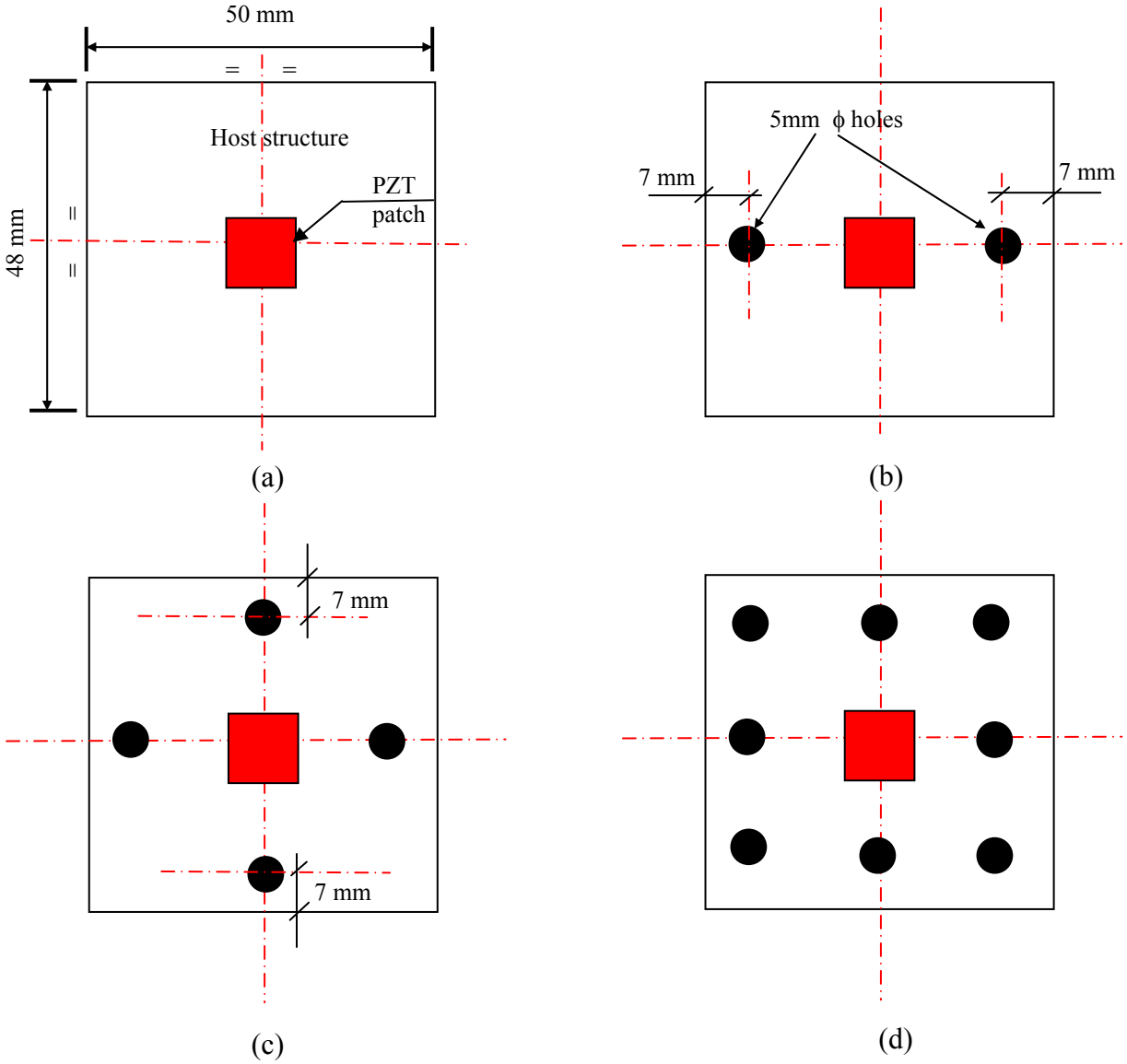

Fig. 17 Levels of damage induced on test specimen (aluminium block).

(a) Pristine state. (b) Incipient damage.

(c) Moderate damage. (d) Severe damage.

Fig. 18 shows the effect of these damages on the identified structural parameters- stiffness and damping, in the frequency range 25-40 kHz. As expected, with damage progression, the stiffness can be observed to reduce and the damping increase. The stiffness reduced by about 12% and the damping increased by about 7% after the incipient damage. Thereafter, with further damage

propagation, very small further drop/increase was observed in these parameters. Fig. 19 shows the effect of these damages on the identified lumped parameters in the 180-200 kHz range. Again, the trend is very consistent with expected behaviour, and much more prominent than for the frequency range 25-40 kHz. With damage progression, the mass and the stiffness can be observed to reduce, and the damping increase. The stiffness reduced gradually- 17% for the incipient damage, 31% for the moderate damage and 47% for the severe damage. The mass similarly reduced with damage severity- 16% for the incipient damage, 28% for the moderate damage and 42% for the severe damage. The damping values (*c* and *C**), on the other hand, increased with damage severity. (Figs. 19c and 19e), though 'c' displayed a slight decrease after the incipient damage. The only exception is found in the parallel stiffness K^*, which remained largely insensitive to all the levels of damage. Contrary to the 25-40 kHz range, the 180-200 kHz range diagnosed the damages much better, as demonstrated by the significant variation in the parameters for moderate and severe damages, in addition to incipient damages.

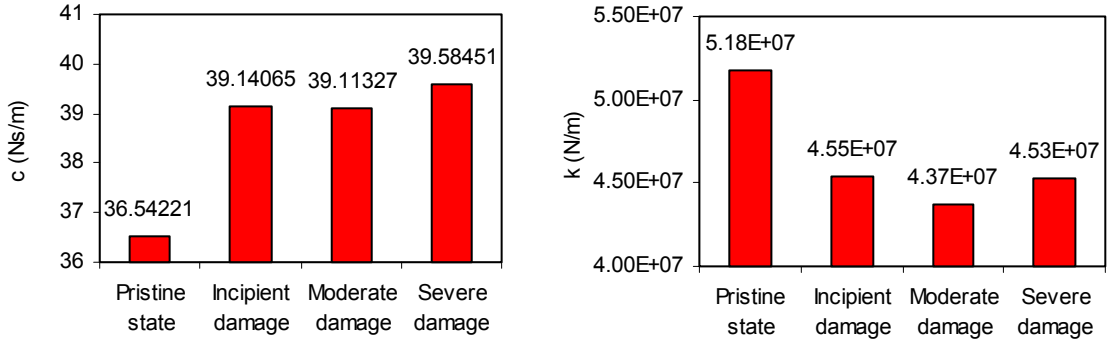

(a) (b)

Fig. 18 Effect of damage on equivalent system parameters in 25-40kHz range.
(a) Equivalent damping constant. (b) Equivalent spring constant.

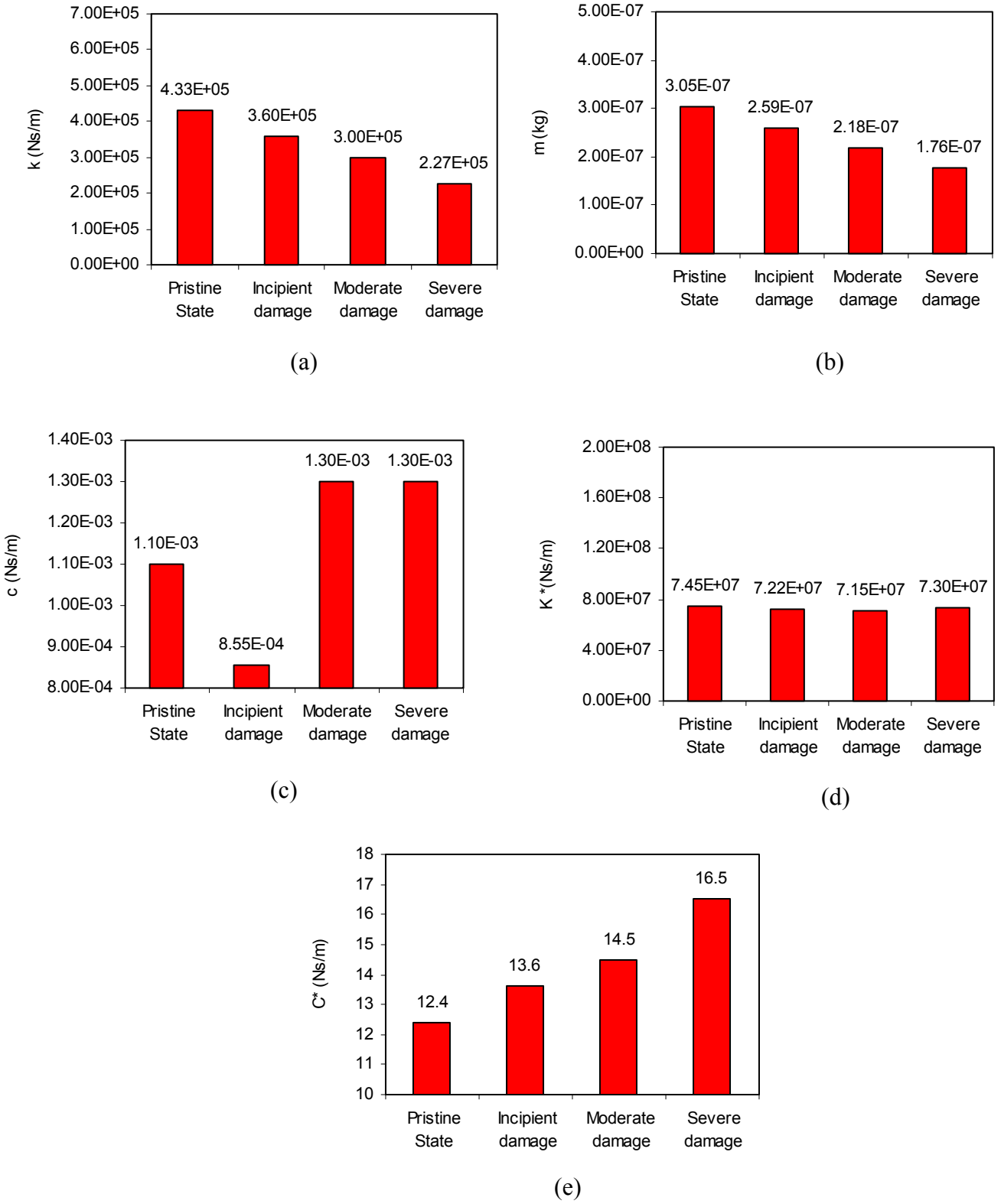

Fig. 19 Effect of damage on equivalent system parameters in 180-200kHz range. (a) Equivalent spring constant. (b) Equivalent mass. (c) Equivalent damping constant. (d) Equivalent additional spring constant. (e) Equivalent additional damping constant.

The higher sensitivity of damage detection in the frequency range180-200 kHz (as compared to 25-40 kHz range) is due to the fact that with increase in frequency, the wavelength of the induced stress waves gets smaller, which are therefore more sensitive to the occurrence of damages. This is also due to the presence of a damage sensitive anti-resonance mode in the frequency range 180-200 kHz (Fig. 16) and its absence in the 25-40 kHz range (Fig. 13). This agrees well with the recommendation of Sun et al. (1995), that to ensure a high sensitivity, the frequency range must contain prominent vibrational modes of the structure. However, it should be noted that in spite of the absence of any major resonance mode in the frequency range 25-40 kHz, the damage is still effectively captured at the incipient stage, although severe damages are not very clearly differentiated from the incipient damage.

Fig. 20 shows a plot between the residual area of the specimen, 'A' (a measure of the residual capacity of the specimen) and the equivalent spring stiffness 'k' identified by the PZT patch. Following empirical relation was found between the two using regression analysis.

$$A = 1874.2 + 0.0021k - 2.02x10^{-9}k^2 \tag{59}$$

This demonstrates that it is possible to calibrate the damage sensitive system parameters with damage and to employ them for damage diagnosis in real scenarios.

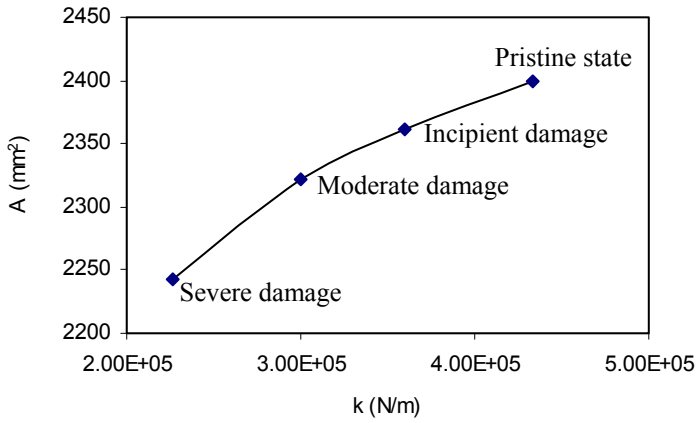

Fig. 20 Plot of residual specimen area versus equivalent spring constant.

This study demonstrates that the proposed method can evaluate structural damages in miniature aerospace components reasonably well. Besides aerospace gadgets, the methodology is also ideal for identifying damages in precision machinery components, turbo machine parts and computer parts such as the hard disks. These components are also quite rigid and exhibit a dynamic behaviour similar to the test structure. The piezo-impedance transducers, because of their miniature characteristics, are unlikely to alter the dynamic characteristics of these miniature systems. They are thus preferred over the other sensor systems and techniques (Giurgiutiu and Zagrai, 2002).

EXTENSION TO DAMAGE DIAGNOSIS OF CIVIL-STRUCTURAL SYSTEMS

In order to demonstrate the feasibility of the proposed methodology for monitoring large civil-structures, the data recorded during the destructive load test on a prototype reinforced concrete (RC) bridge was utilized. The test bridge, shown in Fig. 21, consisted of two spans of about 5m, instrumented with several PZT patches, 10x10x0.2mm in size, conforming to grade PIC 151 (PI Ceramic, 2003). The bridge was subjected to three load cycles so as to induce damages of increasing severity. Details of the instrumentation as well as loading can be found in the references: Soh et al. 2000 and Bhalla, 2001. Root mean square deviation (RMSD) index was used to evaluate damages in the previous study.

The PZT patches detected the presence of surface cracks (see Fig. 21) much earlier than the global condition indicators, such as the load-deflection curve (Soh et al., 2000). Patch 4 was typically selected as a representative PZT patches in the analysis. Fig. 22 shows the impedance spectra of the pristine structure as identified by the PZT patch 4 in the frequency range 120-140 kHz. From this figure, it is observed that the PZT patch has ‘identified’ the structure as a parallel spring-damper combination, the corresponding parameters were worked out as $k = 9.76\text{x}10^7$ N/m

and c = 26.1823 Ns/m. The parameters were also determined for the damaged bridge, after cycles I and II. Fig. 23 provides a look at the associated damage mechanism- '*k*' can be observed to reduce and '*c*' to increase with damage progression. Reduction in the stiffness and increase in the damping is well-known phenomenon associated with crack development in concrete. Damping increased by about 20% after cycle I and about 33% after cycle II. This correlated well with the appearance of cracks in the vicinity of this patch after cycles I and II. Stiffness was found to reduce marginally by about 3% only, after cycle II, indicating the higher sensitivity of damping to damage as compared to stiffness.

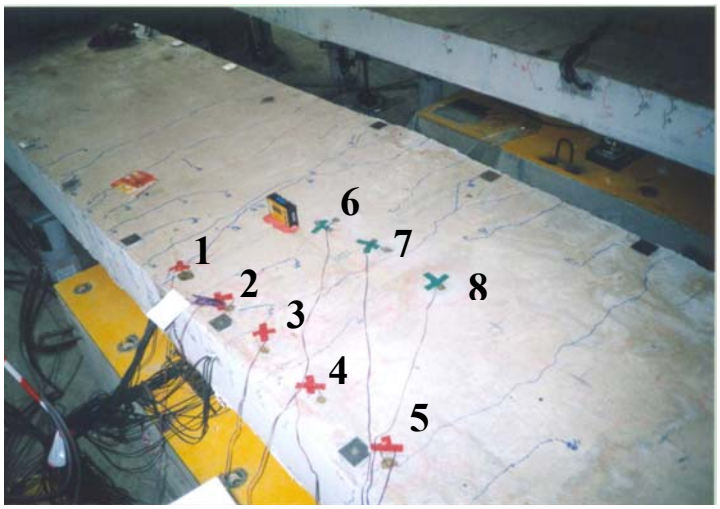

Fig. 21 Damage diagnosis of a prototype RC bridge using proposed methodology.

Thus, the proposed methodology can be easily extended to civil-structures as well. However, it should be noted that owing to the large size of the typical civil-structures, the patch can only 'identify' a localized region of structure, typically representative of the zone of influence of the patch. For large structures, complete monitoring warrants an array of PZT patches. The patches can be monitored on one-by-one basis and can effectively localize as well as evaluate the extent of

damages. The next section will present how the identified system parameters can be calibrated with extent of damage.

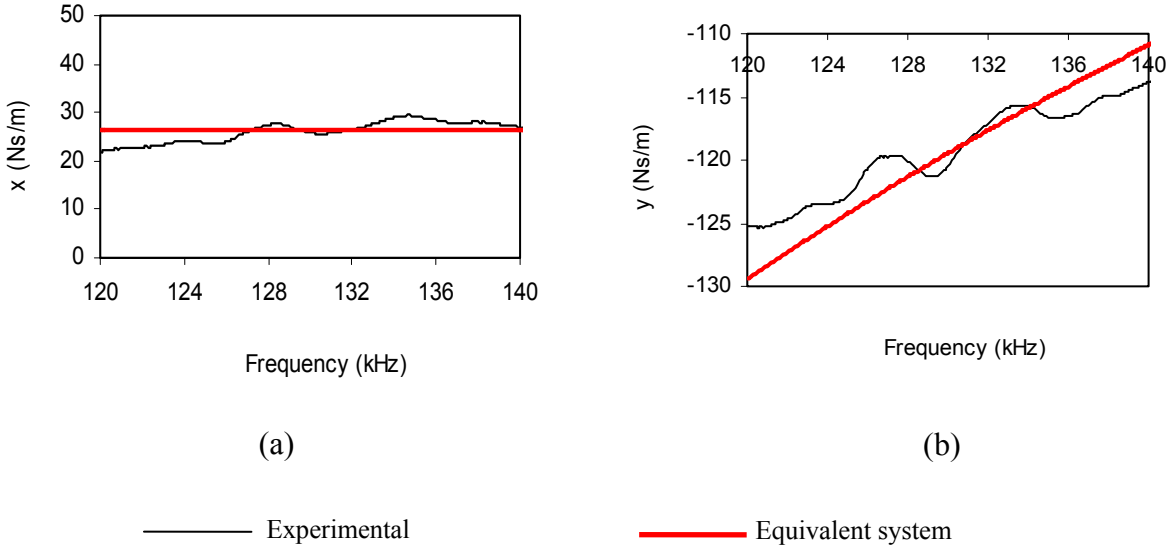

Fig. 22 Mechanical impedance of RC bridge in 120-140 kHz frequency range. The equivalent system plots are obtained for a parallel spring damper combination. (a) Real part (x) vs frequency. (b) Imaginary part (y) vs frequency.

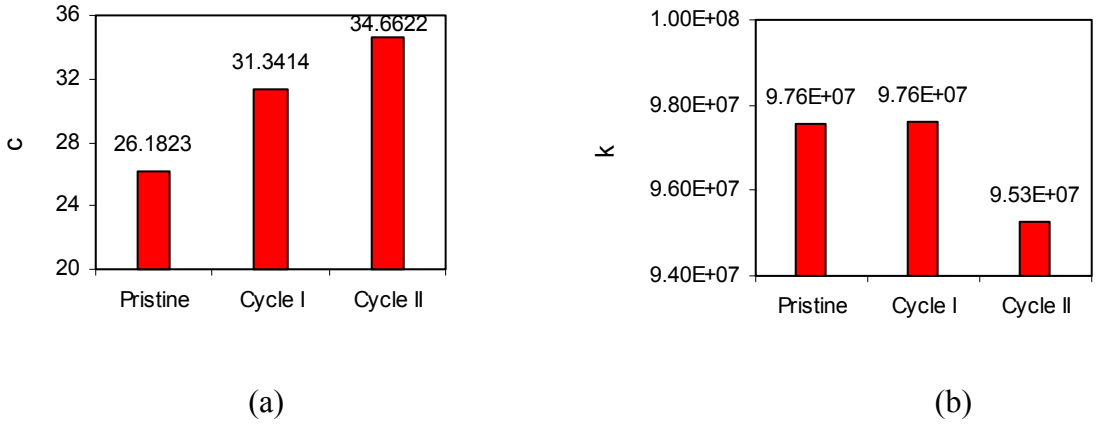

Fig. 23 Effect of damage on equivalent system parameters of RC bridge. (a) Equivalent damping constant. (b) Equivalent spring constant.

CONCRETE STRENGTH PREDICTION USING EMI TECHNIQUE

Conventional Techniques

From the point of view of SHM/ NDE, in addition to damage detection, concrete technologists are interested in concrete strength determination. Special importance is attached to strength determination for concrete because its elastic behaviour and to some extent service behaviour can be easily predicted from the strength characteristics. Although direct strength tests, which are destructive in nature, are excellent for quality control during construction, their main shortcoming is that the tested specimen may not truly represent the concrete in the actual structure. The tests may reflect more the quality of the supplied materials rather than that of the constructed structure. Delays in obtaining results, lack of reproducibility and high costs are few other drawbacks. The NDE methods, on the other hand, aim to measure the strength of concrete in the actual constructed structures. However, these cannot be expected to yield absolute values of strength since they measure some property of concrete from which an estimation of its strength, durability and elastic parameters are estimated. Some common strength measuring techniques for concrete are the rebound hammer test, the penetration test, the resonant frequency test and the ultrasonic pulse velocity test.

The rebound hammer technique predicts concrete strength based on the rebound of a hardened steel hammer dropped on specimen surface from a specified height. Empirical correlations have been established between rebound number and concrete strength. In spite of quick and inexpensive estimation of strength, the results are influenced by surface roughness, type of specimen (shape and size), age, moisture content, and type of cement and aggregate.

Similarly, the penetration technique is based on measuring the depth of penetration of a standard probe, impacted on the surface of the specimen, with a standard energy. However, they

leave a minor damage on concrete surface. The calibration is strongly dependent on the source and type of aggregate used.

The resonant frequency technique is based on the principle that the velocity of sound through a medium is proportional to the Young's modulus of elasticity (and hence strength). The velocity of sound in concrete is obtained by determining the fundamental resonant frequency of vibration of the specimen, which is usually a cylinder (150mm diameter and 300mm length) or a prism (75x75x300mm), by transmitting a mechanical pulse through the specimen. The main drawback of this technique is that it can only be carried out on small lab-sized specimens rather than the structural members in the field.

The ultra sonic pulse velocity (USPV) technique works on the same principle as the resonant frequency method. The only difference is that the velocity of sound is determined by directly measuring the time of travel of the electronically generated longitudinal waves, using a digital meter or a cathode ray oscilloscope. The pulse velocity measurements are correlated with concrete strength, and the error is typically less than 20%. The main limitation of the USPV technique is that the transducers must always be placed on the opposite faces for best results. Very often, this is not possible and this limits the application of the technique. In addition, the correlation between the strength and the velocity is strongly dependent on the type of cement and aggregate.

A detailed review of the conventional NDE techniques for concrete strength prediction is covered by Malhotra (1976) and Bungey (1982).

EMI Technique for Concrete Strength Evaluation

From Eq. (28), the admittance spectra can be obtained for a 'free' and 'clamped' PZT patch, by substituting $Z_{s,eff}$ equal to 0 and ∞ respectively. Fig. 24 displays the admittance spectra (0-1000

kHz), corresponding to these boundary conditions, for a PZT patch 10x10x0.3mm in size, conforming to grade PIC 151 (PI Ceramic, 2003). It is observed from this figure that the three resonance peaks, corresponding to "free-free" planar PZT vibrations, vanish upon clamping the patch. The act of bonding a PZT patch on the surface of concrete will similarly restrain the PZT patch. However, in real life bonding, the level of clamping is somewhat intermediate of these two extreme situations, and hence, the admittance curves are likely to lie in between the curves corresponding to the extreme situations, depending on the stiffness (or strength) of the concrete.

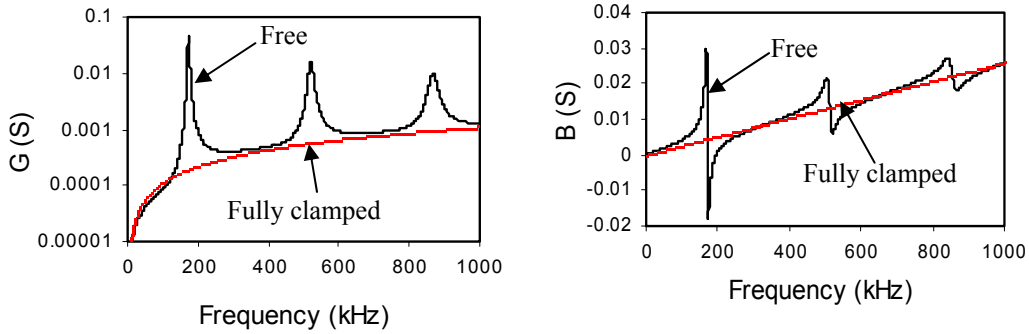

Fig. 24 Admittance spectra for free and fully clamped PZT patches.
(a) Conductance vs frequency. (b) Susceptance vs frequency.

In order to test the feasibility of predicting concrete strength using this principle, identical PZT patches (measuring 10x10x0.3mm, grade PIC 151, key parameters as listed in Table 2), were bonded on the surface of concrete cubes, 150x150x150mm in size. At the time of casting, the proportions of various constituents were adjusted such that different characteristic strengths would be achieved. Same cement as well as aggregate were used for all specimens. After casting, a minimum curing period of 28 days was observed for all except two specimens, for which it was kept one week so as to achieve a low strength at the time of the test. In order to achieve identical bonding

conditions, same thickness of epoxy adhesive layer (RS 850-940, RS Components, 2003) was maintained between the PZT patch and the concrete cube. To ensure this, two optical fibre pieces, 0.125mm in diameter, were first laid parallel to each other on the concrete surface, as shown in Fig. 25 (a). A layer of epoxy was then applied on the concrete surface and the PZT patch was placed on it. Light pressure was maintained over the assembly using a small weight and the set-up was left undisturbed at room temperature for 24 hours to enable curing of the adhesive. The optical fibre pieces were left permanently in the adhesive layer. This procedure ensured a uniform thickness of 0.125mm of bonding layer in all the specimens. Fig. 25(b) shows the finished top surface of a typical specimen with a PZT patch bonded to it.

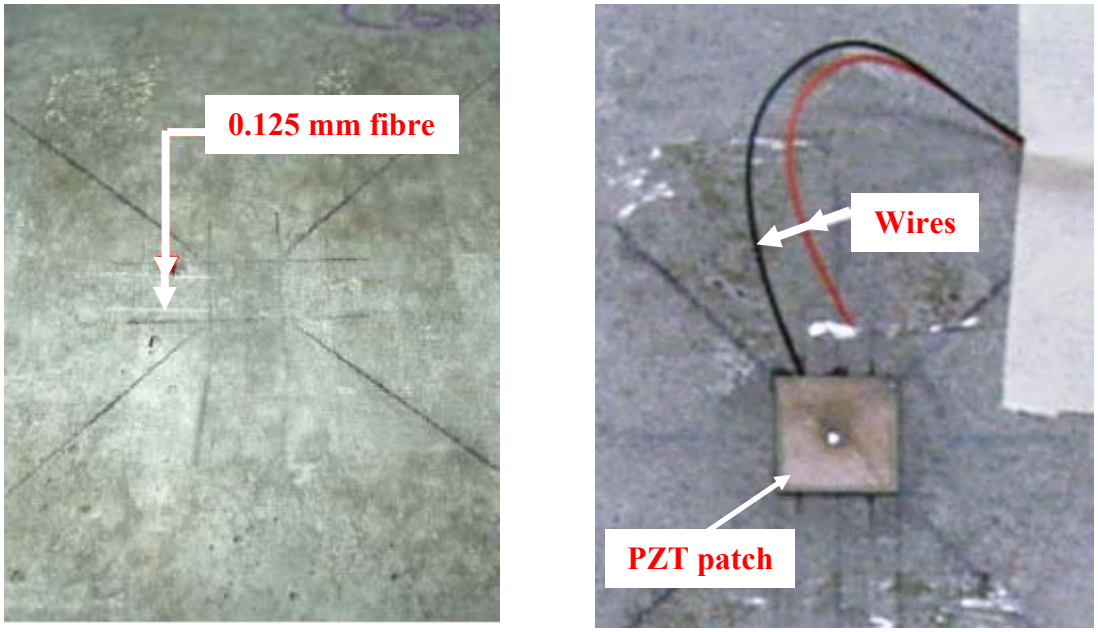

Fig. 25 (a) Optical fibre pieces laid on concrete surface before applying adhesive.
(b) Bonded PZT patch.

Fig. 26 shows the conductance and susceptance plots of the PZT patches bonded to concrete cubes of five different strengths. The strengths indicated on the figure were determined experimentally by subjecting the cubes to cyclic loading on a universal testing machine (UTM). The test procedure will be covered in detail in the next section. The figure also shows the theoretical curves for PZT patch in free as well as clamped conditions.

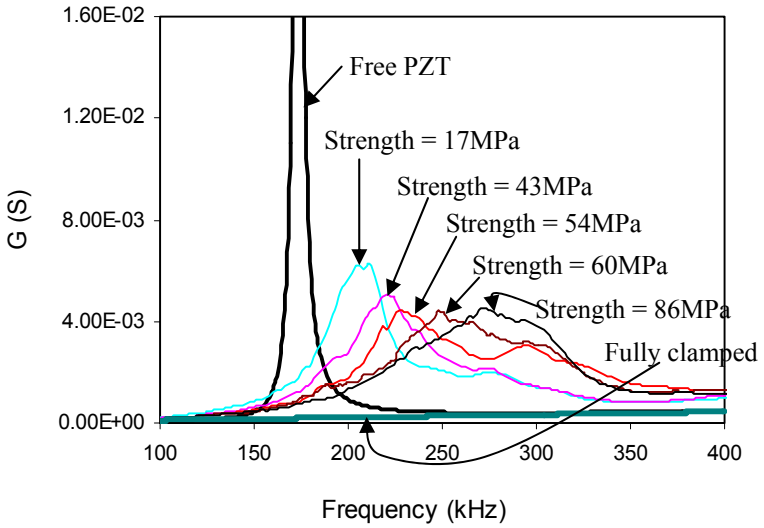

(a)

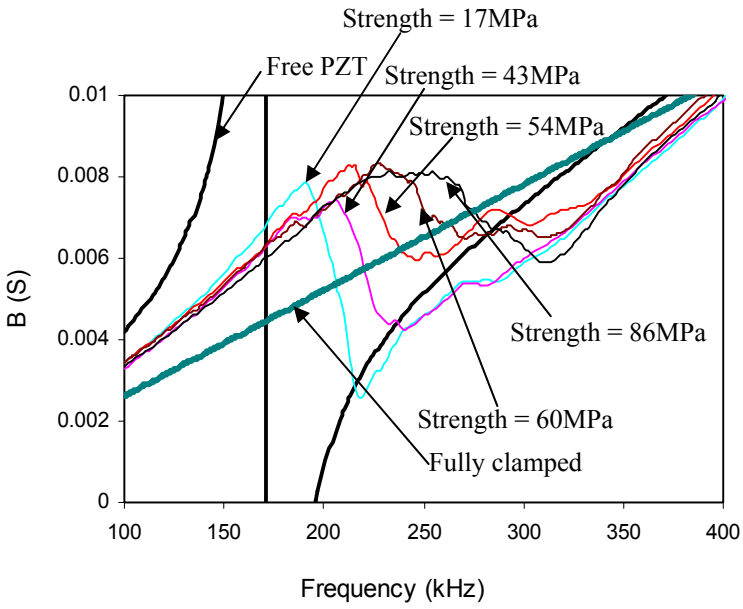

(b)

Fig. 26 Effect of concrete strength on first resonant frequency of PZT patch.

It is apparent from the figures that the first peak frequency (see Fig. 26a) increases with the strength of concrete. This increase is on account of the additional stiffening action due to bonding with concrete, the level of stiffening being related to the concrete strength. Fig. 27 shows a plot between the observed first resonant frequency and measured concrete strength for data pertaining to a total of 17 PZT patches bonded to a total of 11 concrete cubes. At least two cubes were tested corresponding to each strength and the average frequencies were worked out. Free PZT curve was used to obtain the data point corresponding to zero strength. From regression analysis, the following empirical relationship was found between concrete strength (S) and the first resonant frequency

$$S(MPa) = 0.0089 f^2 - 2.6657 f + 196.94 \qquad (60)$$

where the resonant frequency, f, is measured in kHz. This empirical relationship can be used to evaluate concrete strength non-destructively for low to high strength concrete (10MPa < S < 100MPa). It should be mentioned that good correlation was not found between concrete strength and the second and the third peaks (see Fig. 24). This is because at frequencies higher than 500 kHz, the PZT patches become sensitive to their own conditions rather than to the conditions of the structure they are bonded with (Park et al, 2003).

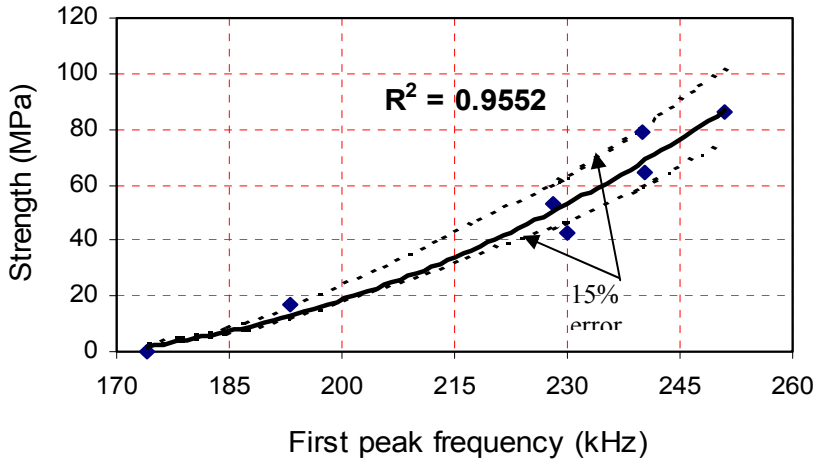

Fig. 27 Correlation between concrete strength and first resonant

Although the tests reported here were carried out on 150mm cubes, the empirical relationship represented by Eq. (60) can be conveniently extended to real-life structures since the zone of influence of the PZT patches is usually very small in concrete. It should also be noted that the strength considered in the present study was obtained by cyclic compression tests, which is expected to be lower than that obtained by the standard testing procedure. Also, the relationship will depend on the type of aggregates, the type of cement, the type and size of PZT patches and the type and thickness of bonding layer. Hence, Eq. (60) cannot be considered as a universal relationship. It is therefore recommended that similar calibration should be first established in the laboratory for the particular concrete under investigation before applying the technique in the field.

The main advantage of the present technique is that there is no requirement of the availability of two opposite surfaces, as in the case of the resonant frequency method and the ultrasonic pulse velocity method. Also, no expensive transducers or equipment are warranted. The next section describes how the EMI technique can be used to predict the extent of damage in concrete.

DAMAGE ASSESSMENT OF CONCRETE USING EMI TECHNIQUE

Selection of Damage Sensitive Parameter

Consider concrete cubes, 150x150x150mm in size, instrumented with square PZT patches (10x10x0.3mm, PIC 151). Using the computational procedure outlined before, the impedance parameters of the cubes were extracted from the admittance signatures of the bonded PZT patches in the frequency range 60-100 kHz. The real and imaginary components of the extracted mechanical impedance were found to exhibit a response similar to that of a parallel spring damper combination, system 1 of Table 3. Typically, for concrete cube with a strength of 43 MPa (designated as C43),

the system parameters were identified to be k = 5.269x10^7 N/m and c = 12.64 Ns/m. Fig. 28 shows the comparison between the experimental impedance spectra and that corresponding to the parallel spring-damper combination with k = 5.269x10^7 N/m and c = 12.64 Ns/m . A good agreement can be observed between the two.

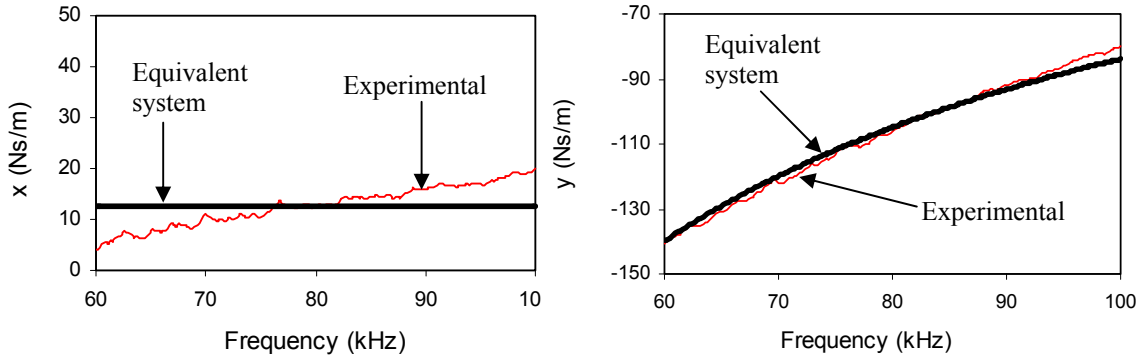

(a) (b)

Fig. 28 Impedance plots for concrete cube C43.

(a) Real component of mechanical impedance (x) vs frequency.

(b) Imaginary component of mechanical impedance (y) vs frequency.

The concrete cubes were then subjected to cyclic loading in an experimental set-up as shown in Fig. 29. In addition to PZT patches, each cube was instrumented with 60mm electrical strain gauges. The PZT patches instrumented on the cubes were wired to an impedance analyzer, which was controlled using the personal computer labelled as PC1 in the figure. The strain gauge was wired to a strain recording data logger, which was in-turn hooked to another personal computer marked PC2, which also controlled the operation of the UTM. The cube was loaded in compression at a rate of 330 kN/min until the first predetermined load. It was then unloaded and the conductance and susceptance signatures were acquired. In the next cycle, the cube was loaded to the next higher level of load and the signatures were again acquired after unloading. This loading, unloading and

signature acquisition process was repeated until failure. Thus, the damage was induced in a cyclic fashion. Typical load histories for four cubes designated as C17 (Strength = 17MPa), C43 (Strength = 43MPa),, C54 (Strength = 54MPa) and C86 (Strength = 86MPa), are shown in Figure 30.

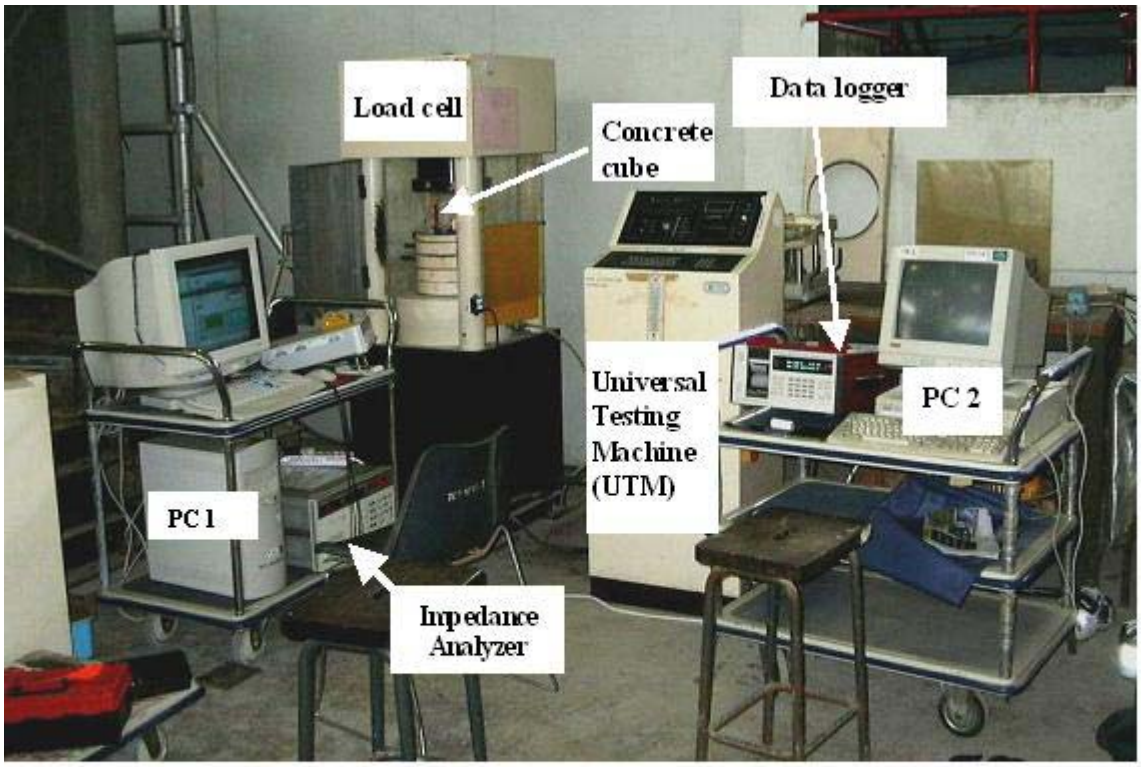

Fig. 29 Experimental set-up for inducing damage on concrete cubes.

From Fig. 30, it is observed that the secant modulus of elasticity progressively diminishes with the number of load cycles. Loss in secant modulus was worked out after each load cycle. At the same time, the extracted equivalent spring stiffness, worked out from the recorded PZT signatures, was found to diminish proportionally. Fig. 31 shows the plots of the loss of secant modulus against the loss of equivalent spring stiffness for four typical cubes C17, C43, C52 and C86. Good

correlation can be observed between the two. From these results, it is thus evident that equivalent spring stiffness can be regarded as a damage sensitive parameter and can be utilized for quantitatively predicting the extent of damage in concrete. It should be noted that the equivalent spring stiffness is obtained solely from the signatures of the piezo-impedance transducers. No information about concrete specimen is warranted *a priori.*

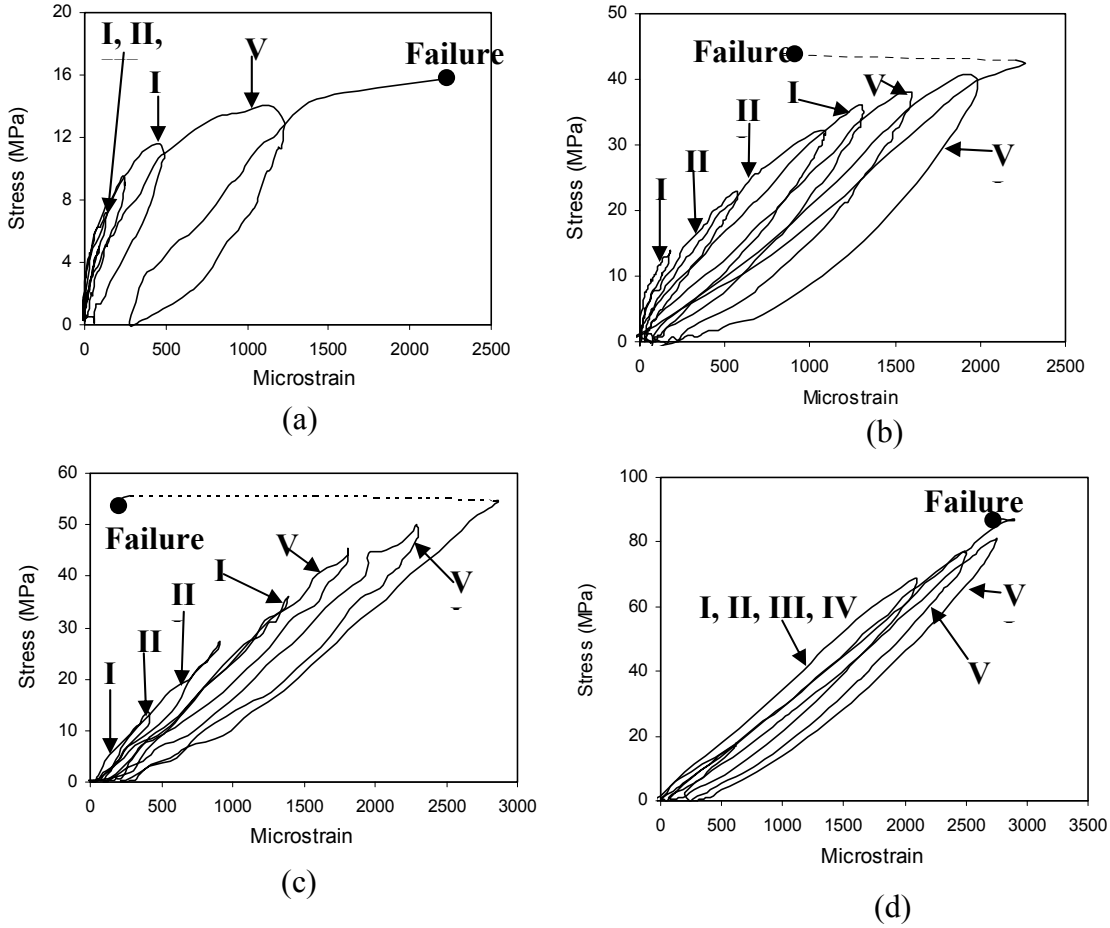

Fig. 30 Load histories of four concrete cubes.
(a) C17 (b) C43 (c) C52 (d) C86

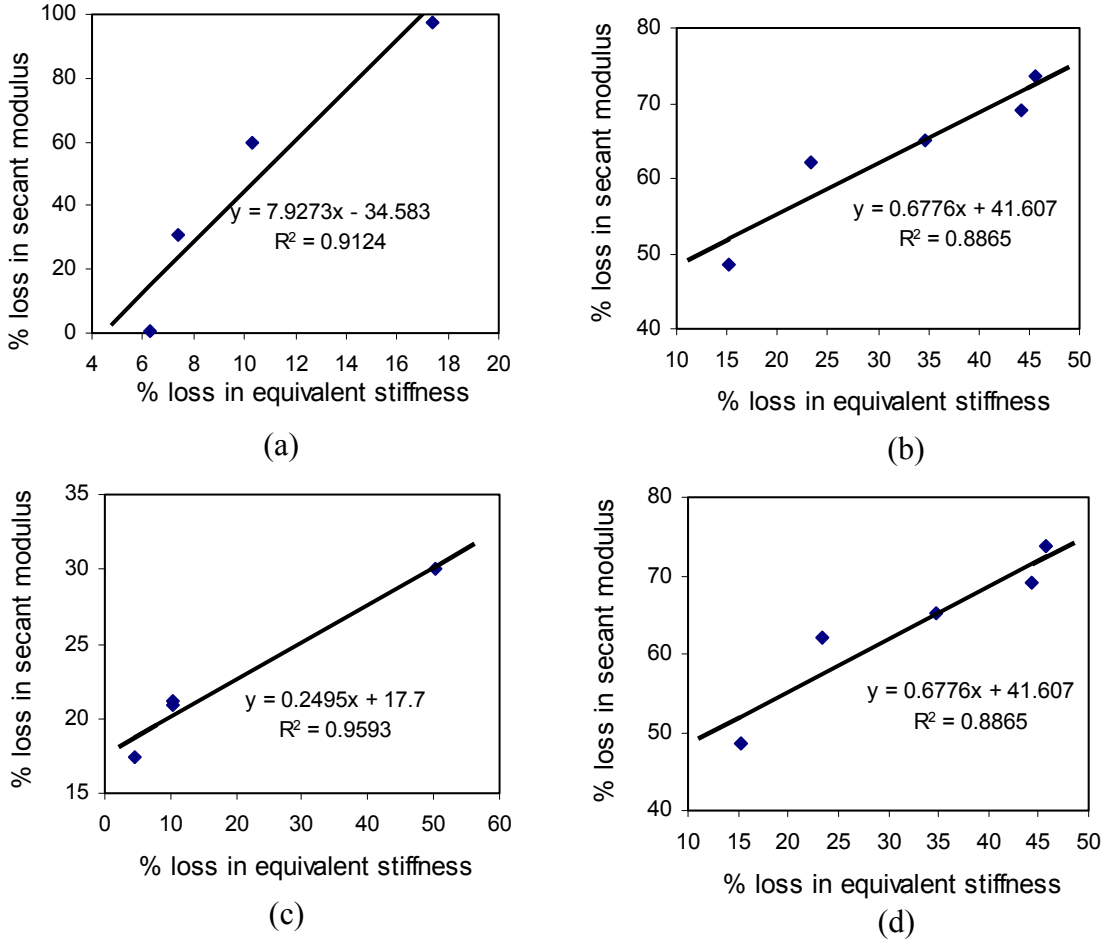

Fig. 31 Correlation between loss of secant modulus and loss of equivalent spring stiffness with damage progression.
(a) C17 (b) C43 (c) C52 (d) C86

It should also be mentioned that the extracted equivalent damping was found to increase with damage. This was as expected, since damping is known to increase with the development of cracks in concrete. Fig. 32 shows typical plot of increase in equivalent damping with damage progression for cube C43. Also shown is the progressive loss in the equivalent stiffness with load ratio. However, in most other cubes, no consistent pattern was observed with respect to damping. Only a

phenomenal increase near failure was observed. For this reason, the equivalent stiffness was selected as the damage sensitive parameter due to its progressive decrement with damage progression and consistent performance.

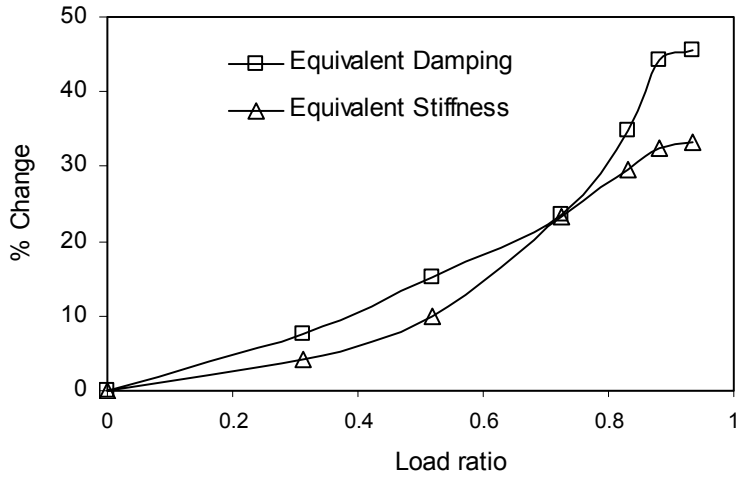

Fig. 32 Changes in equivalent damping and equivalent stiffness for cube C43.

ESTABLISHMENT OF IMPEDANCE-BASED DAMAGE MODEL FOR CONCRETE

Definition of Damage Variable

It has earlier been shown that in the frequency range 60-100 kHz, concrete essentially behaves as a parallel spring damper system. The equivalent stiffness 'k' has been established as a damage sensitive system parameter since it is found to exhibit a reasonable sensitivity to any changes taking place in the system on account of damages. This section deals with calibrating 'k' against damage using the test data obtained from compression tests on concrete cubes.

In general, any damage to concrete causes reduction in the equivalent spring stiffness as identified by the piezo-impedance transducer surface-bonded to it. At i^{th} frequency, the associated damage variable, D_i, can be defined as

$$D_i = 1 - \frac{k_{di}}{k_{oi}} \tag{61}$$

where K_{oi} is the equivalent spring stiffness at the i^{th} measurement point in the pristine state and K_{di} is the corresponding value after damage. It may be noted that $0 < D_i < 1$. Thus, D_i measures the extent of 'softening' of the identified equivalent stiffness due to damage. D_i is expected to increase in magnitude with damage severity. The host structure can be deemed to fail if D exceeds a critical value D_c. However, from the comprehensive tests on concrete cubes, it was found that it is not possible to define a unique value of D_c. This is due to unavoidable uncertainties related to concrete, its constituents and the PZT patches. Therefore it is proposed to define the critical value of the damage variable using the theory of fuzzy sets.

Damage Assessment Based on the Theory of Fuzzy Sets

Scientists and engineers describe complex physical systems by very simple mathematical models, often making considerable idealizations in the process. A practical approach to simplify a complex system is to tolerate a reasonable amount of imprecision, vagueness and uncertainty during the modelling phase. It was this logic which Zadeh (1965) employed when he introduced the notion of fuzzy sets. Fuzzy systems are widely used to model information that is afflicted with imprecision, vagueness, and uncertainty. A fuzzy set is defined as a class of objects with continuum grades of membership. Such a set is characterized by a membership (or characteristic) function, which assigns to each object, a grade of membership ranging from 0 to 1. For example, let $\mathbf{A_f}$ be a fuzzy set of numbers 'much' greater than '1'. Then one can give a precise, albeit subjective value of characterization of **A** by specifying $f_m(x)$. The representative values of such a function might be $f_m(0) = 0$, $f_m(10) = 0.1$ and $f_m(100) = 1.0$ and so on. In general, fuzzy sets merely have an intuitive

basis as a formal description of vague data. They are generally specified by experts directly in an intuitive way. Fuzzy sets were first employed in civil engineering in the late 1970s (e.g. Brown, 1979). Several recent applications of fuzzy sets in civil engineering can be found in the literature, such as Chameau et al. (1983), Dhingra et al. (1992), Valliappan and Pham (1993), Soh and Yang (1996), Wu et al. (1999, 2001) and Yang and Soh (2000).

The membership functions represent the subjective degree of preference of a decision maker within a given tolerance. The determination of a fuzzy membership function is the most difficult as well as the most controversial part of applying the theory of fuzzy sets for modelling engineering problems. Most commonly used shapes are linear, half concave, exponential, triangular, trapezoidal, parabolic, sinusoidal and the extended π-shape (Valliappan and Pham, 1993; Wu et al., 1999, 2001. The choice of the particular shape depends on the opinion of the expert, since there is no hard and fast rule to ascertain which shape is more realistic than others.

If $p(D)$ is the probability density function for describing a failure event D, the failure probability, in general, may be expressed as

$$P_f = \int_S p(D)dD \tag{62}$$

where 'S' is the space of the failure event. However, when the fuzzy set theory is used, a failure event can be treated as a 'fuzzy failure event'. If the membership function is $f_m(D)$, the fuzzy failure probability can be defined as (Wu et al., 1999)

$$P_f = \int_S f_m(D)\,p(D)dD \tag{63}$$

This principle has presently been used in evaluating concrete damage.

Statistical Analysis of Damage Variable for Concrete

Fig. 33 shows the equivalent spring stiffness worked out at various load ratios (applied load divided by failure load) for five cubes labelled as C17, C43, C52, C60 and C86. The damage variables were computed at each frequency in the interval 60-100 kHz, corresponding to each load ratio, for all the five cubes. The mean (μ) and standard deviation (σ) of the damage variable were then evaluated at each damage ratio. Statistical examination of the data pertaining to the damage variables indicated that it followed a normal probability distribution. Fig. 34 shows the empirical cumulative probability distribution of D_i and also the theoretical normal probability distribution for all the cubes at or near failure. The empirical cumulative distribution function was obtained by

$$\hat{F}(x) = \frac{1}{N}\sum_{x_i \le x} n_i \tag{64}$$

where n_i is the frequency of x_i in the data set. The theoretical curves were obtained from the mean μ and the standard deviation σ as

$$F(x) = \int_{v=-\infty}^{v=x} p(v)dv \tag{65}$$

where the probability distribution is given in terms of μ and σ as

$$p(x) = \frac{1}{\sigma\sqrt{2\pi}} e^{-\frac{(x-\mu)^2}{2\sigma^2}} \tag{66}$$

From Fig. 34, it is observed that the distribution of the damage variables fits very well into the normal distribution. The adequacy of the normal distribution was quantitatively tested by Kolmogorov-Smirnov goodness-of-fit test technique (Wu et al., 1999) and the normal distribution was found to be acceptable under a 85% confidence limit for all the cubes.

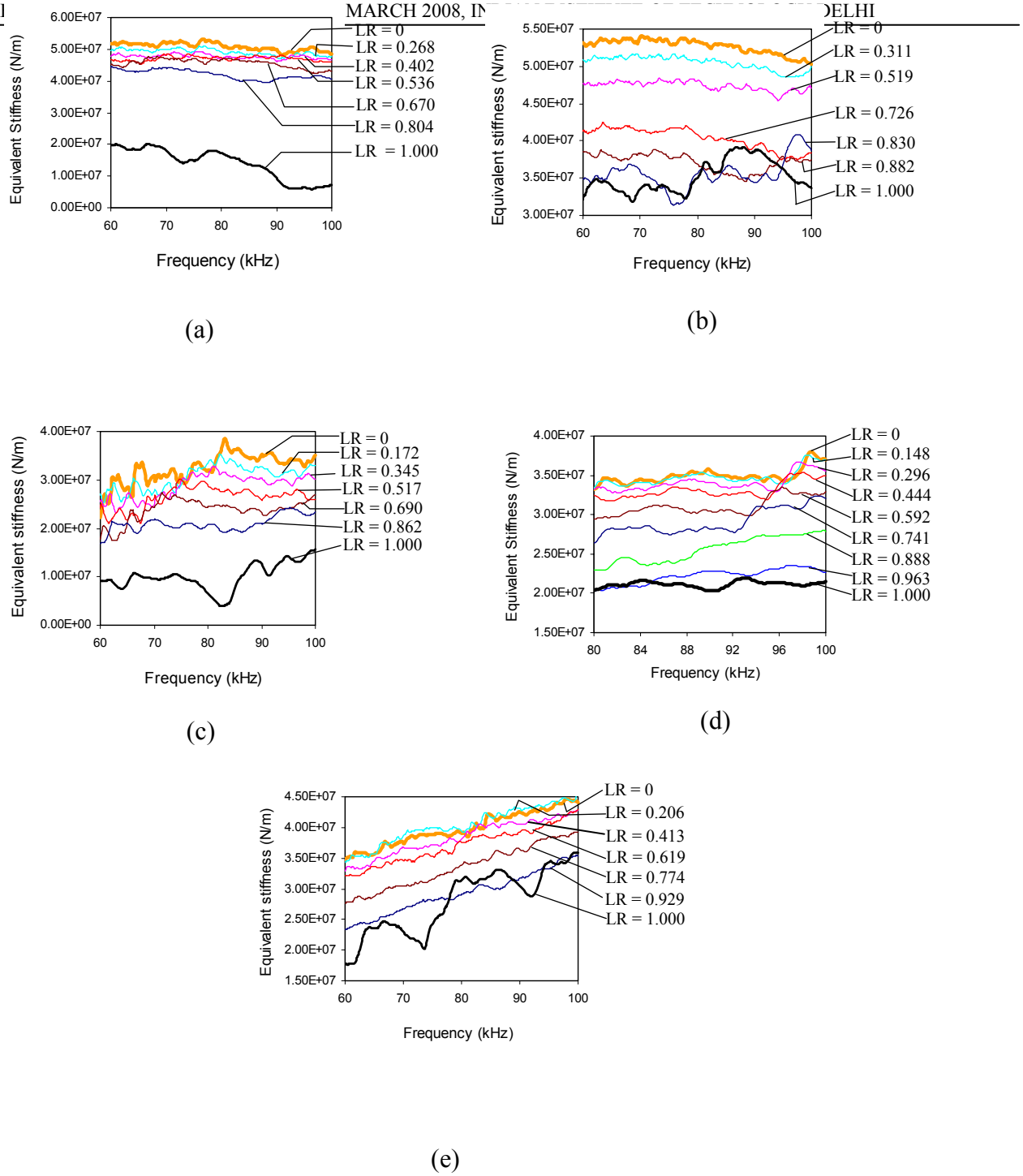

Fig. 33 Effect of damage on equivalent spring stiffness (LR stands for 'Load Ratio').
(a) C17 (b) C43 (c) C52 (d) C60 (e) C86

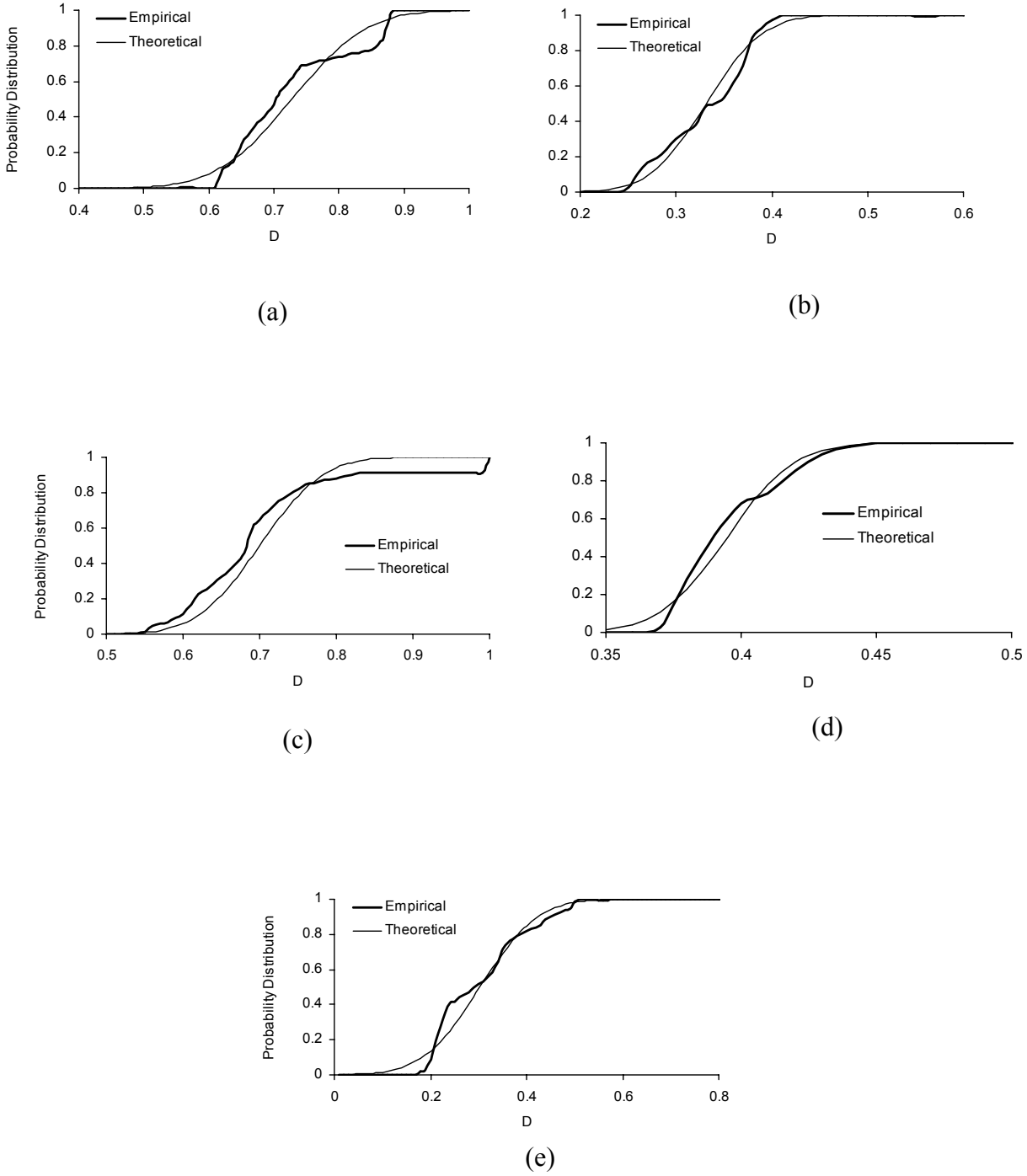

Fig. 34 Theoretical and empirical probability density functions near failure.
(a) C17 (b) C43 (c) C52 (d) C60 (e) C86

Computation of Fuzzy Failure Probability

From the theory of continuum damage mechanics, an element can be deemed to fail if $D > D_c$. As pointed out earlier, instead of defining a unique value of the critical damage variable D_c, a fuzzy definition is employed in our study to take the uncertainties into account. A fuzzy region may be defined in the interval (D_L, D_U) where D_L and D_U respectively represent the lower and the upper limit of the fuzzy region (Valliappan and Pham, 1993; Wu et al., 1999). $D > D_U$ represents a failure region with 100% failure possibility and $D < D_L$ represents a safe region with 0% failure possibility. Within the fuzzy or the transition region, that is $D_L < D < D_U$, the failure possibility could vary between 0% and 100%. A characteristic or a membership function f_m could be defined ($0 < f_m(D) < 1$) to express the grade of failure possibility within the region (D_L, D_U). The fuzzy failure probability can then be determined, from Eq. (63), as

$$P_f = P(D \geq D_C) = \int_{D=0}^{D=1} f_m(D)\, p(D)\, dD \tag{67}$$

where $p(D)$ is the probability density function of the damage variable D, which in the present case complies with normal distribution. Based on observations during concrete cube compression tests, D_L and D_U were chosen as 0.0 and 0.40 respectively. Further, from practical experience, a sinusoidal membership function given by the following equation was adopted

$$f_m = 0.5 + 0.5 \sin\left[\frac{\pi}{(D_U - D_L)}(D - 0.5D_U - 0.5D_L)\right] \tag{68}$$

Making use of this membership function, the fuzzy failure probability (FFP) was worked out for the five concrete cubes at each load ratio.

A load ratio of 0.4 can be regarded as incipient damage since the concrete is expected to be under ‘working loads’. All concrete cubes were found to exhibit a fuzzy failure probability of less

than 30% at this load ratio. Similarly, at a load ratio of 0.8, the concrete is expected to be under 'ultimate loads'. For this case, all the cubes exhibited a fuzzy failure probability of greater than 80% irrespective of strength. This is shown in Fig. 35. Fig. 36 shows the FFP of the cubes at intermediate stages during the tests. Based on minute observations made during testing of the concrete cubes, the following classification of damage is recommended based on FFP.

FFP < 30%	Incipient Damage (Micro-cracks)
30% < FFP < 60%	Moderate damage (Cracks start opening up)
60% < FFP < 80%	Severe damage (large visible cracks)
FFP > 80%	Failure imminent

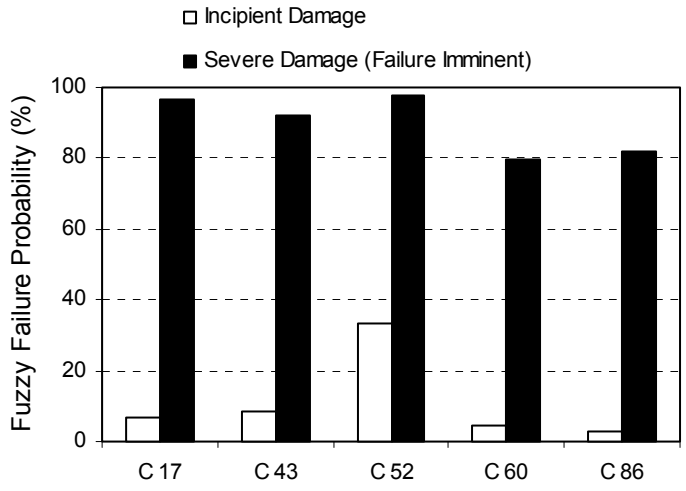

Fig. 35 Fuzzy failure probabilities of concrete cubes at incipient damage level and at failure stage.

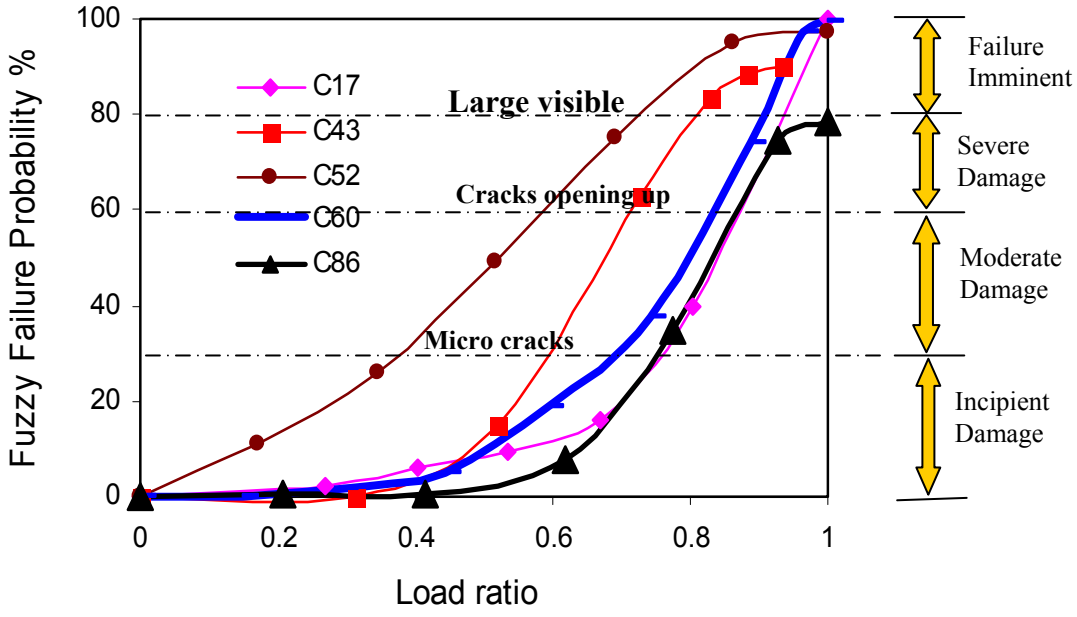

Fig. 36 Fuzzy failure probabilities of concrete cubes at various load levels.

Thus, the fuzzy probabilistic approach quantifies the extent of damage on a uniform 0-100% scale. This can be employed to evaluate damage in real-life concrete structures. From these results, it is observed that all the PZT patches exhibited more or less a uniform behaviour with damage progression, although the strength of concrete cubes varied from as low as 17 MPa to as high as 86 MPa. The PZT patches were subjected to a wide range of mechanical stresses and strains during the tests. At a load ratio of 1.0, almost same order of FFP is observed, irrespective of the absolute load or stress level (for example 17 MPa for C17 and 86 MPa for C86). In general, the PZT material shows very high compressive strength, typically over 500 MPa, and also exhibits a linear stress-strain relation up to strains as high as 0.006. In the experiments conducted on concrete cubes, the strain level never exceeded 0.003 (50% of the linear limit). Fig. 37 shows close ups of the cubes after the tests. The results show that the sensor response reflected more the damage to the

surrounding concrete rather than damage to the patches themselves. In general, we can expect such good performance in materials like concrete characterized by low strength as compared to the PZT patches. Hence, damage to concrete is likely to occur first, rather than the PZT patch. Further, though the cubes were tested in compression, the same fuzzy probabilistic damage model can be expected to hold good for tension also.

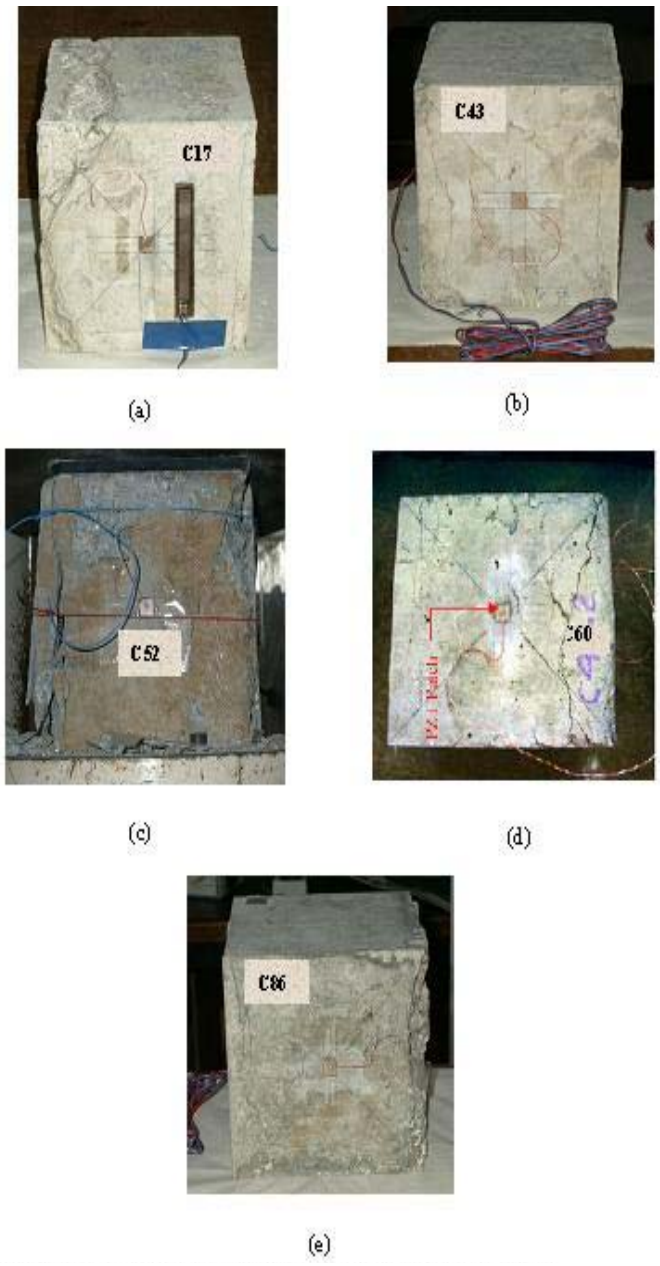

Fig. 37 Concrete cubes after the test. (a) C 17 (b) C43 (c) C53 (d) C60 (e) C86

MONITORING CONCRETE CURING USING EXTRACTED IMPEDANCE PARAMETERS

In order to evaluate the feasibility of the 'identified' spring stiffness in monitoring curing of concrete, a PZT patch, 10x10x0.3mm in size (grade PIC 151, PI Ceramic) was instrumented on a concrete cube, measuring 150x150x150mm in size. A bond layer thickness of 0.125mm was achieved with the aid of optical fibre pieces. The instrumentation was done three days after casting the cube. The PZT patch was periodically interrogated for the acquisition of electrical admittance signatures and this was continued for a period of one year. Figs. 38 and 39 respectively show the short term and the long term effects of ageing on the conductance signatures in the frequency range 100-150 kHz. It is observed that with ageing, the peak is shifting rightwards and at the same time getting sharper. This trend is exactly opposite to the trend observed during compression tests, where the peaks tend to shift leftwards (Bhalla, 2001). The rightward shifting of the resonance peak indicates that the stiffness (and hence the strength) is increasing with time. The phenomenon of peak getting sharper with time suggests that the material damping is reducing (concrete was initially 'soft'). It is a well-known fact that moisture in the concrete matrix is the major contributor to damping (Malhotra, 1976). Hence, with curing, as moisture content drops, the damping in concrete tends to decrease.

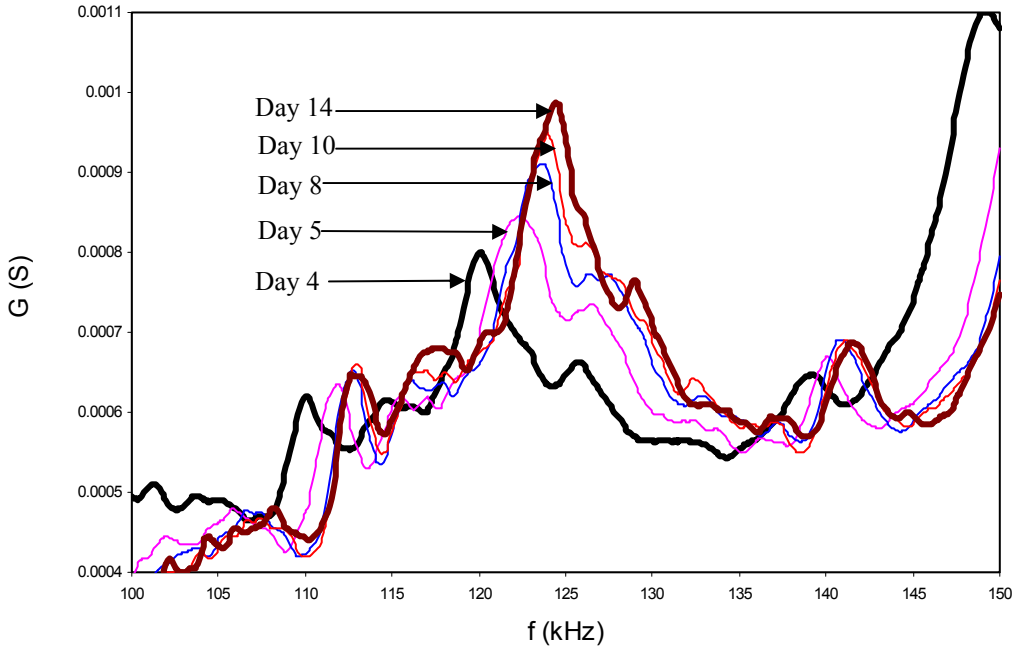

Fig. 38 Short-term effect of concrete curing on conductance signatures.

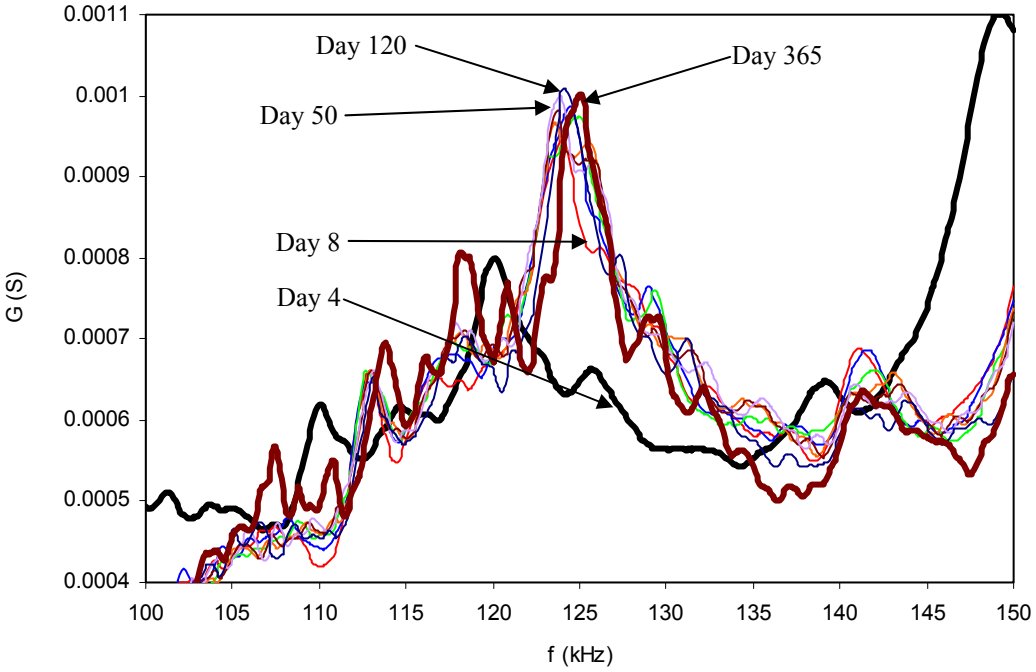

Fig. 39 Long-term effect of concrete curing on conductance signatures.

It should be noted that the particular peak in this figure is the resonance peak of the structure. It should not be confused with the resonance peak of the PZT patch, such as that shown in Fig. 26. As concrete strength increases, the resonance peak of the PZT patch subsides due to the predominance of structural interaction (Fig. 26). However, the structural resonance peak (Figs. 38 and 39), on the other hand, tends to get sharper. In other words, increasing structural stiffness tends to 'dampen' PZT resonance and 'sharpen' the host structure's resonance peak.

In order to quantitatively describe the phenomenon, the equivalent stiffness of the cube was worked out in the frequency range 60-100 kHz using the signatures of the bonded PZT patch. The results are presented in Fig. 40. It can be observed from the figure that as the curing progressed, the equivalent spring stiffness increased, reaching an asymptotic value, about 115% higher than the first recorded value (four days after casting). After 28 days, the increase in the equivalent spring stiffness was about 80%. On comparison with similar monitoring using the ultrasonic pulse velocity technique (Malhotra, 1976), it is found that the present approach is more powerful in monitoring concrete curing. For example, Malhotra (1976) reported an increase of only 7% in the ultrasonic pulse velocity between day 4 and day 10. On the other hand, in our experiment, a much higher increase of 60% was observed between day 4 and day 10. This establishes the superior performance of the EMI technique for monitoring concrete curing. This technique can be applied in the construction industry to decide the time of removal of the form work. It can also be employed to determine the time of commencement of prestressing operations in the prestressed concrete members. In addition, numerous other industrial processes, which involve such curing (of materials other than concrete, such as adhesives), can also benefit from it.

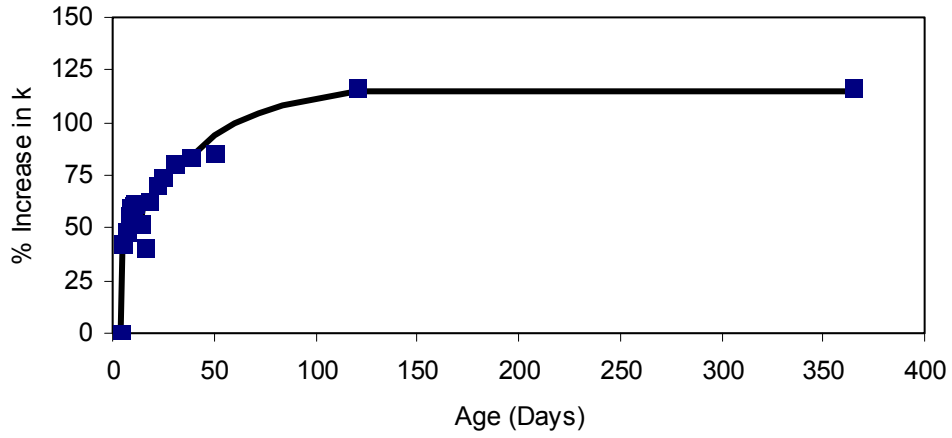

Fig. 40 Effect of concrete curing on equivalent spring stiffness.

PRACTICAL ISSUES RELATED TO EMI TECHNIQUE

PZT transducers are relatively new to the SHM/NDE engineers, who are more accustomed to using the conventional sensors such as strain gauges and accelerometers. They are often skeptical about the reliability of the signature based EMI technique. It is often argued that if the signatures are not repeatable enough over long periods of time, it could be very confusing for the maintenance engineers to make any meaningful interpretation about damage. No study has so far been reported to investigate this vital practical issue. Therefore, in this research, an experimental investigation, spanning over two months, was carried on a PZT patch bonded to an aluminum plate, 200x160x2mm .The PZT patch was periodically scanned for over two months. Very often, the wires from the patches to the impedance analyzer were detached and reconnected during the experiments. Fig. 41 shows the conductance signatures of the first patch over the two-month duration. Good repeatability is clearly evident from this figure. Standard deviation was determined for this set of signatures at each frequency step, which worked out to be 4.36×10^{-6}S (Seimens) on an average against a mean value of 2.68×10^{-4} S. Hence, the normalized standard deviation (average standard

deviation divided by mean) worked out to be 1.5% only, which shows that the repeatability of the signatures was excellent over the period of experiments.

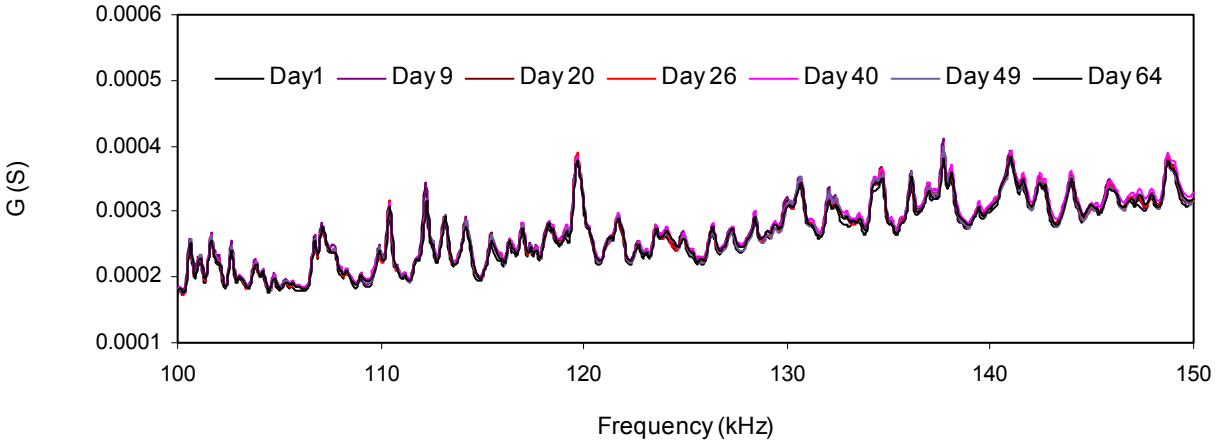

Fig. 41 A set of conductance signatures of PZT patch bonded to an aluminium specimen spanning over two months.

If piezo-impedance transducers are to be employed for SHM/ NDE of real-life structures, they are bound to be influenced by environmental effects, such as temperature fluctuations and humidity. Temperature effects have been studied by many researchers in the past (e.g. Sun et al., 1995; Park et al., 1999) and algorithms for compensating these have already been developed. However, no study has so far been undertaken to investigate the influence of humidity on the signatures. An experiment was therefore conducted to study this effect. The PZT patch bonded to the aluminium plate was soaked in water for 24 hours and its signatures were recorded before as well as after this exercise (excess water was wiped off the surface before recording the signature). Figs. 42(a) and (b) compare the conductance and susceptance signatures respectively for two

conditions. That humidity has exercised adverse effect on the signatures is clearly evident by the substantial vertical shift in the conductance signature (Fig. 42a). From Eq. (28), it is most probable that the presence of humidity has significantly increased the electric permittivity of the patch. This experiment suggests that a protection layer is necessary to protect the PZT patches against humidity in the actual field applications.

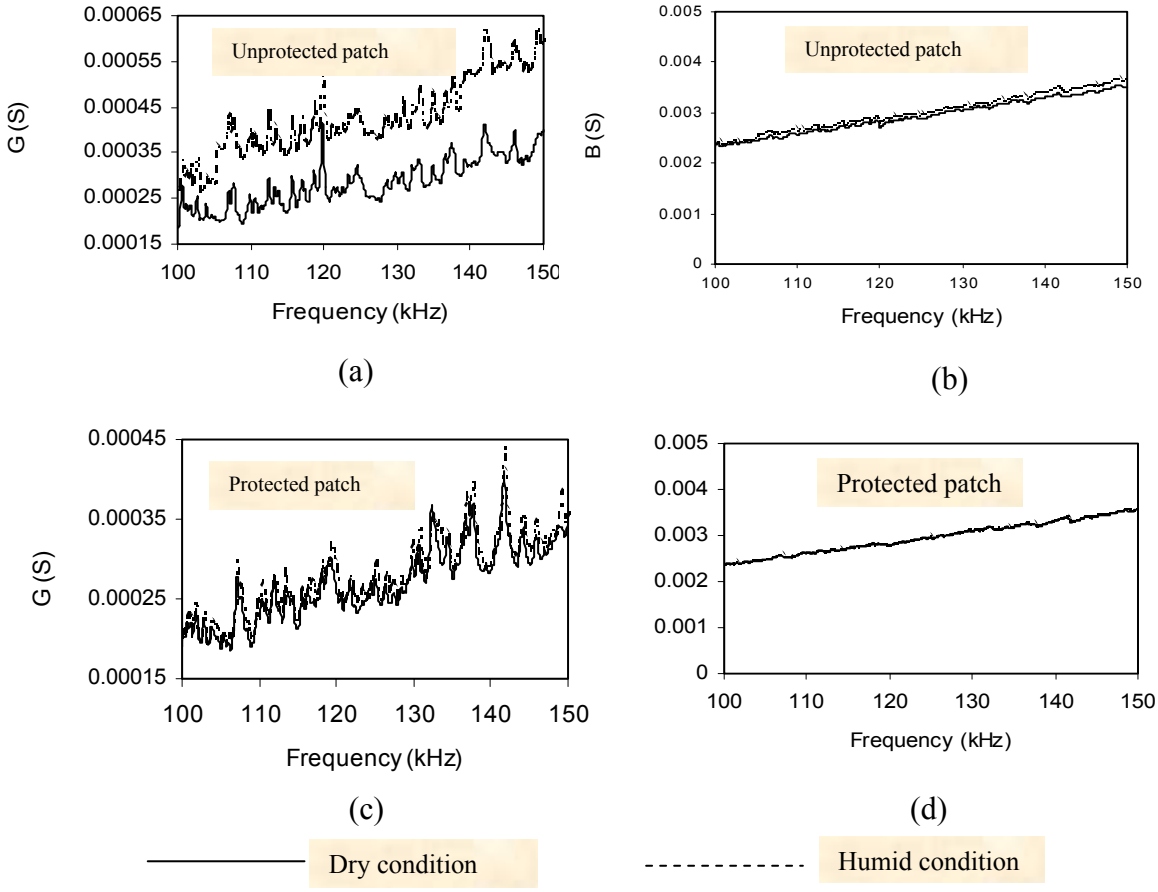

Fig. 42 Effect of humidity on signature.

(a) Unprotected patch: G-plot. (b) Unprotected patch: B-plot.

(c) Protected patch: G-plot. (d) Protected patch: B-plot.

Silicon rubber was chosen as a candidate protective material since it is known to be a good water proofing material, chemically inert, and at the same time a very good electric insulator. Besides, it is commercially available as paste which can be solidified by curing at room temperature. To evaluate the protective strength of silicon rubber, another PZT patch instrumented on the same aluminium plate was covered with silicon rubber coating (grade 3140, Dow Corning Corporation, 2003). The previous experiment (i.e. soaking with water for 24 hours) was repeated. Figs. 42 (c) and (d) compare the signatures recorded from this patch in the dry state as well as humid state. It is found that there is very negligible change in the signatures even after long exposure to humid conditions. Hence, silicon rubber is capable of protecting PZT patches against humidity. It should be mentioned that commercially available packaged QuickPack® actuators (Mide Technology Corporation, 2004) are also likely to be robust against humidity, though no study has been reported so far. However, the packaging itself increases the cost by at least 10 times. The proposed protection, using silicon rubber, on the other hand, offers a simple and economical solution to the problem of humidity. In addition, it has also been found that the presence of the silicon layer has only a negligible effect on the sensitivity of the PZT patch.

CONCLUSIONS

This paper described the recent developments in structural identification, health monitoring and non-destructive evaluation using surface bonded piezo-impedance transducers. In addition to the existing PZT-structure interaction models, a new effective impedance based impedance model proposed by the authors was also described. As opposed to the previous impedance-based models, the new model condenses the two-directional mechanical coupling between the PZT patch and the host structure into a single impedance term. The model was verified on a representative aerospace structural component over a frequency range of 0-200 kHz. The new impedance formulations can be

conveniently employed to extract the 2D mechanical impedance of any 'unknown' structure from the admittance signatures of a surface-bonded PZT patch. Thus, the unknown structure can be identified and its damage can be parametrically quantified. Proof-of-concept applications of the proposed structural identification and health monitoring methodology were reported on structures ranging from precision machine and aerospace components to large civil-structures. Since the dynamic characteristics of the host structure are not altered by small sized PZT patches, a very accurate structural identification is therefore possible by the proposed method. The piezo-impedance transducers can be installed on the inaccessible parts of crucial machine components, aircraft main landing gear fitting, turbo-engine blades, space shuttles and civil-structures to perform continuous real-time SHM. The equivalent system is identified from the experimental data alone. No analytical/ numerical model is required as a prerequisite. Apart from NDE, the proposed model can be employed in numerous other applications, such as predicting system's response, energy conversion efficiency and system power consumption.

The paper also reported calibration of piezo-impedance transducers for damage assessment of concrete. In the frequency range 60-100 kHz, concrete essentially behaves as a parallel spring damper combination. The equivalent spring stiffness was found to reduce and the damping increase with damage progression. A fuzzy probability based damage model was proposed based on the extracted equivalent stiffness from the tests conducted on concrete. This enabled the calibration of the piezo-impedance transducers in terms of damage severity and can serve as a practical empirical phenomenological damage model for quantitatively estimating damage severity of concrete.

A new experimental technique was reported for determining the in situ concrete strength non-destructively using the EMI principle. The new technique is much superior than the existing strength prediction techniques, such as the ultrasonic techniques. In addition, the paper demonstrated

the feasibility of monitoring curing of concrete using the EMI technique, which was found to share a sensitivity much higher than the conventional NDE techniques. The paper also addressed key practical issues related to the implementation of the EMI technique for NDE of real-life structures. The results of the repeatability study, which extended over a period of two months, demonstrated that the PZT patches exhibit excellent repeatable performance and are reliable enough for monitoring real-life structures. However, the signatures are at the same time highly prone to deviation by humidity. Silicon rubber was experimentally shown to be a sound material for protecting PZT patches against humidity. The new developments reported here could improve SHM/ NDE, using the EMI technique, for a wide spectrum of structural systems.

REFERENCES

1. Agilent Technologies (2003), Test and Measurement Catalogue, USA.
2. ANSYS Reference Manual; Release 5.6 (2000), ANSYS Inc., Canonsburg, PA, USA.
3. Ayres, J. W., Lalande, F., Chaudhry, Z. and Rogers, C. A. (1998), "Qualitative Impedance-Based Health Monitoring of Civil Infrastructures", Smart Materials and Structures, Vol. 7, No. 5, pp. 599-605.
4. Bhalla, S. (2001), "Smart System Based Automated Health Monitoring of Structures", M.Eng. Thesis, Nanyang Technological University, Singapore.
5. Bhalla, S., Naidu, A. S. K. and Soh, C. K. (2002), "Influence of Structure-Actuator Interactions and Temperature on Piezoelectric Mechatronic Signatures for NDE", Proceedings of ISSS-SPIE International Conference on Smart Materials, Structures and Systems, edited by B. Dattaguru, S. Gopalakrishnan and S. Mohan, 12-14 December, Bangalore, Microart Multimedia Solutions (Bangalore), pp. 213-219.
6. Bhalla, S. and Soh, C. K. (2003), "Structural Impedance Based Damage Diagnosis by Piezo-Transducers", Earthquake Engineering and Structural Dynamics, Vol. 32, No. 12, pp. 1897-1916.
7. Bhalla, S. and Soh, C.K. (2004a), "High Frequency Piezoelectric Signatures for Diagnosis of Seismic/ Blast Induced Structural Damages", NDT&E International, Vol. 37, No. 1, pp. 23-33.
8. Bhalla, S. and Soh, C.K. (2004b), "Structural Health monitoring by Piezo-Impedance Transducers: Modeling", Journal of Aerospace Engineering, ASCE, Vol. 17, No. 4, pp. 154-165..

9. Bhalla, S. and Soh, C.K. (2004c), "Structural Health monitoring by Piezo-Impedance Transducers: Applications", Journal of Aerospace Engineering, ASCE, Vol. 17, No. 4, pp. 166-175.
10. Bhalla, S. and Soh C. K. (2007) "Progress in Structural Health Monitoring and Non-Destructive Evaluation Using Piezo-Impedance Transducers", Smart Materials and Structures: New Research, Nova Science Publishers, Inc. , New York, pp. 177-228.
11. **Bhalla, S.,** Yang, Y. W., Zhao, J. and Soh, C. K. *(*2005), "Structural Health Monitoring of Underground Facilities- Technological Issues and Challenges", Tunnelling and Underground Space Technology ,Vol. 20, No. 5 (September), pp. 487-500.
12. Brown, C. B. (1979), "A Fuzzy Safety Measure", Journal of Engineering Mechanics Division, ASCE, Vol. 105, pp. 855-872.
13. Bungey, J. H. (1982), The Testing of Concrete in Structures, Surrey University Press.
14. Chameau, J. L. A, Alteschaeffl, A., Michael, H. L. and Yao, J. P. T. (1983), "Potential Applications of Fuzzy Sets in Civil Engineering", International Journal of Man-Machine Studies, Vol. 19, pp. 9-18.
15. Crawley, E. F. and de Luis, J. (1987), "Use of Piezoelectric Actuators as Elements of Intelligent Structures", AIAA Journal, Vol. 25, No. 10, pp. 1373-1385.
16. Dhingra, A. K., Rao, S. S. and Kumar, V. (1992), "Non-linear Membership Functions in Multi-Objective Fuzzy Optimization of Mechanical and Structural Systems", AIAA Journal, Vol. 30, No. 1, pp. 251-260.
17. Dow Corning Corporation (2003), http://www.dowcorning.com
18. Fairweather, J. A. (1998), "Designing with Active Materials: An Impedance Based Approach", Ph.D. Thesis, Rensselaer Polytechnic Institute, New York.

19. Giurgiutiu, V. and Rogers, C. A., (1997), "Electromechanical (E/M) Impedance Method for Structural Health Monitoring and Non-Destructive Evaluation", Proceedings of International Workshop on Structural Health Monitoring, edited by F. K. Chang, Stanford University, Stanford, California, September 18-20, Technomic Publishing Co., pp. 433-444.
20. Giurgiutiu, V. and Rogers, C. A. (1998), "Recent Advancements in the Electro-Mechanical (E/M) Impedance Method for Structural Health Monitoring and NDE", Proceedings of SPIE Conference on *Smart Structures and Integrated Systems,* San Diego, California, March, SPIE Vol. 3329, pp. 536-547.
21. Giurgiutiu, V. and Zagrai, A. N. (2002), "Embedded Self-Sensing Piezoelectric Active Sensors for On-Line Structural Identification", Journal of Vibration and Acoustics, ASME, Vol. 124, pp. 116-125.
22. Gudra, T. and Stawiski, B. (2000), "Non-Destructive Strength Characterization of Concrete Using surface waves", NDT&E International, Vol. 33, pp. 1-6.
23. Hixon, E.L. (1988), "Mechanical Impedance", Shock and Vibration Handbook, edited by C. M. Harris, 3rd ed., Mc Graw Hill Book Co., New York, pp. 10.1-10.46.
24. Hewlett Packard (1996), HP LF 4192A Impedance Analyzer, Operation Manual, Japan.
25. Hey, F., Bhalla, S. and Soh, C. K. (2006), "Optimized Parallel Interrogation and Protection of Piezo-Transducers in Electro-Mechanical Impedance Technique", Journal of Intelligent Material Systems and Structures, Vol. 17, No. 6 (June), pp.457-468.
26. Ikeda, T. (1990), Fundamentals of Piezoelectricity, Oxford University Press, Oxford.
27. Liang, C., Sun, F. P. and Rogers, C. A. (1993), "An Impedance Method for Dynamic Analysis of Active Material Systems", Proceedings of AIAA/ ASME/ ASCE/ Material Systems, La- Jolla, California, pp. 3587-3599.

28. Liang, C., Sun, F. P. and Rogers, C. A. (1994), "Coupled Electro-Mechanical Analysis of Adaptive Material Systems- Determination of the Actuator Power Consumption and System Energy Transfer", Journal of Intelligent Material Systems and Structures, Vol. 5, pp. 12-20.
29. Lim Y. Y., **Bhalla, S.** and Soh, C. K. (2006), "Structural Identification and Damage Diagnosis Using Self-Sensing Piezo-Impedance Transducers", Smart Materials and Structures, Vol. 15, No. 4 (August), pp. 987-995.
30. McCann, D. M. and Forde, M. C. (2001), "Review of NDT Methods in the Assessment of Concrete and Masonary Structures", NDT & E International, Vol. 34, pp. 71-84.
31. Malhotra, V. M. (1976), Testing Hardened Concrete: Nondestructive Methods, American Concrete Institute (ACI) Monograph No. 9.
32. Mide Technology Corporation (2004), http://www.mide.com
33. Pandey, A. K., Biswas, M. and Samman, M. M. (1991), "Damage Detection from Changes in Curvature Mode Shapes", Journal of Sound and Vibration, Vol. 145, No. 2, pp. 321-332.
34. Pandey, A. K. and Biswas, M. (1994), "Damage Detection in Structures Using Changes in Flexibility", Journal of Sound and Vibration, Vol. 169, No. 1, pp. 3-17.
35. Park, G., Kabeya, K., Cudney, H. H. and Inman, D. J. (1999), "Impedance-Based Structural Health Monitoring for Temperature Varying Applications", JSME International Journal, Vol. 42, No. 2, pp. 249-258.
36. Park, G. (2000), "Assessing Structural Integrity Using Mechatronic Impedance Transducers with Applications in Extreme Environments", Ph.D. Dissertation, Virginia Polytechnic Institute and State University, Blacksburg, VA.

37. Park, G., Cudney, H. H. and Inman, D. J. (2000), "Impedance-Based Health Monitoring of Civil Structural Components", Journal of Infrastructure Systems, ASCE, Vol. 6, No. 4, pp. 153-160.

38. Park, G., Cudney, H. H. and Inman, D. J. (2001), "Feasibility of Using Impedance-Based Damage Assessment for Pipeline Structures", Earthquake Engineering and Structural Dynamics, Vol. 30, No. 10, pp. 1463-1474.

39. Park, G., Sohn, H., Farrar, C. R. and Inman, D. J. (2003), "Overview of Piezoelectric Impedance-Based Health Monitoring and Path Forward", The Shock and Vibration Digest, Vol. 35, No. 5, pp. 451-463.

40. PI Ceramic (2003), Product Information Catalogue, Lindenstrabe, Germany, http://www.piceramic.de.

41. RS Components (2003), Northants, UK, http://www.rs-components.com.

42. Shah, S. P., Popovics, J. S., Subramaniam, K. V. and Aldea, C. M. (2000), "New Directions in Concrete Health Monitoring Technology", Journal of Engineering Mechanics, ASCE, Vol. 126, No. 7, pp. 754-760.

43. Soh, C. K., Tseng, K. K. H., Bhalla, S. and Gupta, A. (2000), "Performance of Smart Piezoceramic Patches in Health Monitoring of a RC Bridge", Smart Materials and Structures, Vol. 9, No. 4, pp. 533-542.

44. Soh, C. K. and Yang, J. P. (1996), "Fuzzy Controlled Genetic Algorithm Search for Shape Optimization", Journal of Computing in Civil Engineering, ASCE, Vol. 10, No. 2, pp. 143-150.

45. Stubbs, N. and Kim, J. T. (1994), "Field Verification of a Nondestructive Damage Localization and Severity Estimation Algorithm", Texas A & M University Report prepared for New Mexico State University.

46. Sun, F. P., Chaudhry, Z., Rogers, C. A., Majmundar, M. and Liang, C. (1995) "Automated Real-Time Structure Health Monitoring via Signature Pattern Recognition", edited by I. Chopra, Proceedings of SPIE Conference on *Smart Structures and Materials,* San Diego, California, Feb.27-Mar1, SPIE vol. 2443, pp. 236-247.

47. Valliappan, S. and Pham, T. D. (1993), "Fuzzy Finite Element Analysis of a Foundation on an Elastic Soil Medium", International Journal for Numerical and Analytical Methods on Geomechanics, Vol. 17, pp. 771-789.

48. Wu, C. Q., Hao, H. and Zhou, Y. X. (1999), "Fuzzy-Random Probabilistic Analysis of Rock Mass Responses to Explosive Loads", Computers and Geotechnics, Vol. 25, No. 4, pp. 205-225.

49. Wu, C. Q., Hao, H., Zhao, J. and Zhou, Y. X. (2001), "Statistical Analysis of Anisotropic Damage of the Bukit Timah Granite", Rock Mechanics and Rock Engineering, Vol. 34, No. 1, pp. 23-38.

50. Yang, Y. W. and Soh, C. K. (2000), "Fuzzy Logic Integrated Genetic Programming for Optimization and Design", Journal of Computing in Civil Engineering, ASCE, Vol. 14, No. 4, pp. 249-254.

51. Yang , Y. W., **Bhalla, S.**, Wang, C., Soh C. K. and Zhao J. (2007) "Monitoring of Rocks Using Smart Sensors," Tunnelling and Underground Space Technology, Vol. 22, No. 2 (March) pp. 206-221.

52. Zadeh, L. A. (1965), "Fuzzy Sets", Information Control, Vol. 8, pp. 338-353.

53. Zhou, S., Liang, C. and Rogers, C. A. (1995), "Integration and Design of Piezoceramic Elements in Intelligent Structures", Journal of Intelligent Material Systems and Structures, Vol. 6, No. 6, pp. 733-743.

54. Zhou, S. W., Liang, C. and Rogers C. A. (1996), "An Impedance-Based System Modeling Approach for Induced Strain Actuator-Driven Structures", Journal of Vibrations and Acoustics, ASME, Vol. 118, No. 3, pp. 323-331.

55. Zimmerman, D. C. and Kaouk, M. (1994), "Structural Damage Detection Using a Minimum Rank Update Theory", Journal of Vibration and Accoustics, Vol. 116, pp. 222-231.